ENG 284-(EQC 1991/66)

Elongation in Reinforced Concrete Frames

K T Douglas, assisted by Dr B J Davidson (Auckland Uniservices Ltd)

ENG 284

UniServices

Auckland UniServices Limited

Our Ref: 4020

ELONGATION IN REINFORCED CONCRETE FRAMES

AUCKLAND UNISERVICES LIMITED

a wholly owned company of

THE UNIVERSITY OF AUCKLAND

PRIVATE BAG 92019

AUCKLAND

Report prepared for:

Earthquake & War Damages Commission
PO Box 31342
Lower Hutt

Consultants:

K.T. Douglas
supervised by
Dr B.J. Davidson
Department of Civil Engineering
University of Auckland

Date: November 1992

ELONGATION IN REINFORCED CONCRETE FRAMES

-by-

K.T. Douglas

School of Engineering

Report No. 526

Supervised by

Dr. B.J. Davidson

Department of Civil Engineering

University of Auckland

Private Bag

Auckland

New Zealand

November 1992

Abstract

A 'finite element structure', which models the observed behaviour of plastic hinge zones of reinforced concrete frame structures, was developed and implemented into a nonlinear dynamic computer program.

A series of static and dynamic analytic tests were then carried out on a number of reinforced concrete frame structures to assess the performance of the hinge structure, the magnitude of the elongation arising in the beams and the effects of this elongation on the response of the structures.

Acknowledgements

I would like to thank the War and Earthquake Damages Committee for the financial assistance provided for this report.

I wish also to express my sincere thanks to my supervisor Dr. B.J. Davidson, and his colleague Prof. R.C. Fenwick for their much valued guidance and input during the course of this study.

Finally, I would like to thank Eileena Sucich for typing the majority of this report and Martyn Nash for his help and encouragement.

Contents

Chapter 4 Portal Frame Analyses

Chapter 5 Multi-Storey Frame Analyses

Chapter 6 Summary and Conclusions

Chapter 1

INTRODUCTION

1.1 The Elongation Phenomenon

In order to survive a severe earthquake most seismically resistant structures are designed using a combination of both strength and ductility. Ductile structures have the ability to dissipate energy when loaded into the inelastic region by deforming without collapsing. To achieve this ductility selected parts of the structure are designed to withstand inelastic deformation, while the remainder of the structure is proportioned to ensure that the inelastic actions occur only in the chosen areas. These areas are known as plastic hinge zones, and have a large influence on the seismic behaviour of the structure.

It is usual practice to design multi-storey frame structures to develop a beam sway failure mode so that most of the potential plastic hinge zones are located in the beams. Consequently once yielding has occurred, the dynamic performance of the structure is largely influenced by the load-deformation characteristics of the plastic hinge zones that form in the beams.

During severe earthquakes two different types of plastic hinge zones can form, they are referred to as reversing and uni-directional plastic hinges. In reinforced concrete beam structures, the large inelastic deformations that develop in both of these hinge forms cause the associated beams to elongate.

Design engineers have known about this elongation phenomenon for some time, but have considered it to be a second order effect, consequently its influence on the performance of seismically designed reinforced concrete structures has been neglected. Recent test results [1,2,3] however, have shown that member elongation effects can be expected to have a major influence on the seismic performance of reinforced concrete structures with respect to; the support of precast floor units and external cladding panels, the performance of columns in frame structures, the behaviour of diaphragms and walls in mixed wall structures, and the seismic gap provided between buildings.

It is therefore important to obtain a better understanding of the mechanisms of this growth phenomenon and to develop a method of predicting both the behaviour and consequences of reinforced concrete beam elongation.

1.2 Scope of this Report

A plastic hinge finite element structure which models the reinforced concrete beam elongation phenomenon was developed and implemented into the two dimensional nonlinear dynamic computer program DRAIN-2DX.

The hinge structure was then used to predict the magnitude of growth of the beams in a number of frames and the effect of this elongation on the overall seismic response of the structures.

Chapter 2

THEORY

2.1 The Mechanics of Elongation

2.1.1 Introduction

When a reinforced concrete beam cracks in flexure, unless the beam is restrained, elongation of the member will result. If the beam is designed to behave in a ductile manner this elongation becomes more pronounced due to the inelastic actions that occur in the plastic hinge zones.

In beams subjected to inelastic cyclic displacements, two types of plastic hinge can develop depending on the magnitude of the spread load supported along their length. In frame structures where beams support a critical load, W_{crit} or less (see equation 2.1), along their length, the inelastic deformations that result involve the formation of both positive and negative rotations at the column faces. Such hinges are referred to as 'reversing plastic hinges'. If however the beams support a load that is greater than the critical load, 'uni-directional plastic hinges' result, with negative rotations accumulating at the column faces and positive rotations accumulating in the spans of the beams.

$$W_{crit} = 2(M_a + M_b)/l \qquad (2.1)$$

In the above equation M_a and M_b are the maximum positive and negative flexural strengths at the ends of the member, and l, is the clear span between the column faces as shown in Fig. 2.1

During severe earthquakes the high inelastic rotations that develop in both hinge forms inevitably lead to elongations of the associated members.

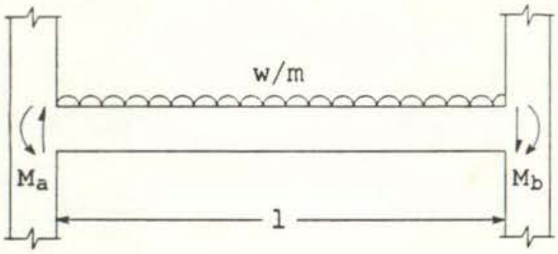

Fig. 2.1 Critical Uniformly Distributed Load

2.1.2 The Formation and Behaviour of Uni-directional Plastic Hinges

Uni-directional plastic hinges mostly develop in beams which have been designed for the dual purpose of providing both gravity and seismic resistance. They form as illustrated in Figs. 2.2a and 2.2b.

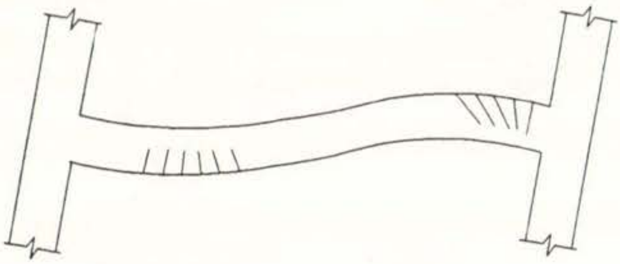

Fig. 2.2a Sway to the Right

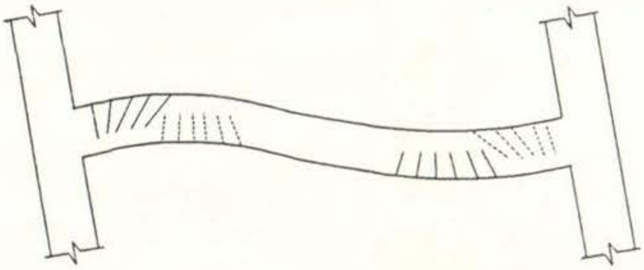

Fig. 2.2b Sway to the Left

As the beam frame structure sways to the right, a negative moment forms at the right hand column face while a positive moment forms in the span of the beam on the left hand side of the centre-line. With the reversal of the sway direction, two new hinge zones are formed. A negative moment rotation at the left hand column face and a positive moment rotation in the span of the beam on the right hand side of the centre line. Every change in sway direction causes an increase in the hinge rotations resulting in an accumulation of negative moment rotations at the column faces and positive moment rotations in the spans of the beams. The high rotations produced cause member elongation by the mechanism illustrated in Fig. 2.3.

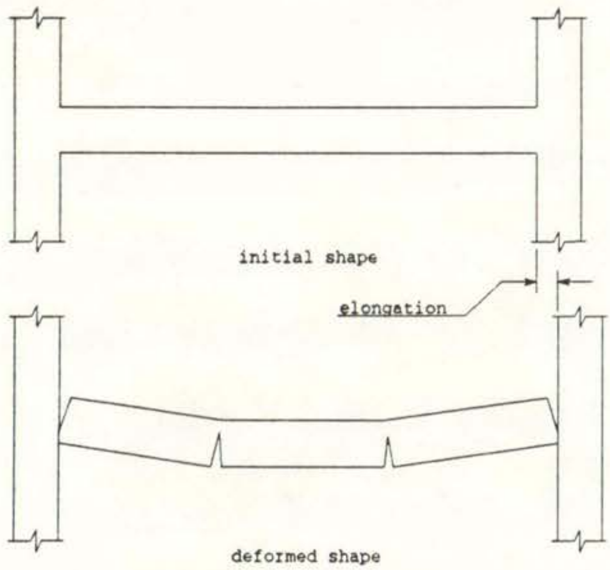

Fig. 2.3 Elongation Mechanism

Tests carried out at Auckland University [2,3] on beam-column sub-assemblies which formed uni-directional plastic hinge zones concluded that because strains in the compression zone reinforcement are small they can for practical purposes be taken as zero. Hence the elongation of a beam, measured at mid-depth is given by the expression:

$$\text{elongation} = \Sigma\theta(d - d')/2 \tag{2.2}$$

where $(d - d')$ is the distance between the centroids of the flexural reinforcement and $\Sigma\theta$ is the sum of the plastic hinge rotations. Comparisons with elongation values derived from the above expression and measured experimental values showed good agreement, except that the elongation is overestimated when the reinforcement starts to buckle [3].

2.1.3 The Formation and Behaviour of Reversing Plastic Hinges

Reversing plastic hinge zones can be expected to form in the beams of frame structures as illustrated in Figs. 2.4a and 2.4b providing the maximum moments form at the ends of a member and none of the positive bending moment flexural reinforcement is terminated near the column faces.

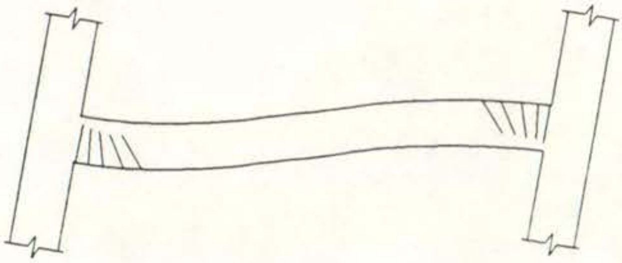

Fig. 2.4a Sway to the Right

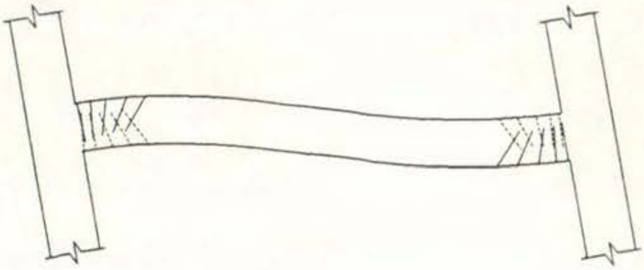

Fig. 2.4b Sway to the Left

As the structure sways to the right positive and negative moments form in the beam at the left and right column faces respectively. With the reversal of sway comes an associated reversal of direction of the inelastic rotations such that a positive moment forms at the right column face, while a negative moment forms at the left column face.

Tests [1,2,3] carried out on the formation and consequences of reversing plastic hinges have concluded that with cyclic load reversal, tension zone reinforcement yields to a greater extent than compression zone reinforcement. Consequently reinforcement that has yielded in tension in the previous cycle, does not yield back to the same magnitude as the tension yield, when in the compression loading phase. So with continued cyclic loading the compression zone reinforcement will effectively lengthen and the cracks in the compression zone will remain open. This was found to be a major contributing factor to the axial extension of the member [1,2,3]. The elongation action described above, is primarily due to a truss like shear resistance mechanism (see Figs. 2.5a and 2.5b) which develops in the hinge zones. In order for the mechanism to remain in equilibrium, once the intersecting diagonal cracks have formed, the compression force sustained by the reinforcement must be smaller than the opposing tension force.

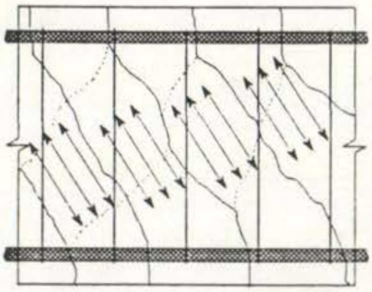

Fig. 2.5a Crack and Diagonal Force Pattern

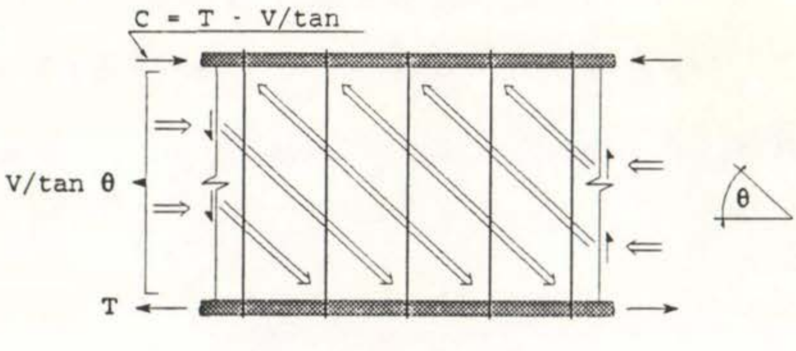

Fig. 2.5b Truss Mechanism

Another factor that was found to contribute to the member elongation was a wedging action that is produced by dislocated aggregate particles which fall in the cracks of the member during cyclic loading. This action hinders complete crack closure and enhances the tensile yielding elongation phenomenon.

For the reversing hinge the elongation at mid-depth has been empirically derived [1,2,3] as;

$$\text{elongation} = \Sigma\theta(d - d')/2 + e \tag{2.3}$$

where (d - d′) is the distance between the centroids of the flexural reinforcement, $\Sigma\theta$ is the sum of the plastic hinge rotations and e is the elongation of the longitudinal reinforcement in the compression zones of the plastic hinges.

2.2 Modelling the Elongation Phenomenon

2.2.1 Introduction

In this initial research project it was decided to model the elongation which resulted from flexural behaviour in the hinge region. Thus in order to best represent the mechanics of plastic hinge elongation with respect to flexure only, a composite element structure was created for implementation in the nonlinear dynamic computer program DRAIN-2DX. It employs two new finite elements which represent the more complex inelastic stress-strain properties of the steel and concrete within the plastic hinge zones. As a result, both reversing and uni-directional plastic hinges can be modelled.

2.2.2 DRAIN-2DX

Because of the complexity of seismic design, it is important for research purposes to obtain detailed information about the probable response of a structure during earthquake loading. As this response involves inelastic actions it is essential that an inelastic model is used. DRAIN- 2DX is a general purpose computer program developed specifically for the two dimensional analysis of elastic and inelastic structural systems. It has a flexible coding format which allows the incorporation of new element types and features with minimum adjustments.

Static Analyses Procedure

For static analyses DRAIN-2DX employs an 'event-to-event' calculation scheme. An event is defined to be a significant change in stiffness usually as a result of yielding, buckling or unloading. Associated with each new event is a yield code, indicating the type of yielding that is taking place, and an event code, describing the new event in terms of the element behaviour, for example; unloading from tension, or yielding in compression. For the event-to-event procedure, automatically determined load increments are used so that the next event is always reached and the element stiffness is updated. Thus if the load-displacement relationship is multi-linear, the solution does not diverge from the equilibrium path and there is no unbalanced load. The mechanics of this event-to-event calculation scheme are as follows;

Consider for example the multi-linear load-displacement relationship shown in Fig. 2.6a. If a load increment, ΔR, is applied to the element when it is at displacement, r_o, and sustaining load, R_o, then a corresponding displacement increment, Δr_1, is calculated using stiffness K_1 (see Fig 2.6b). Because this displacement increment exceeds that required to reach the next event at A, both it and the load increment are scaled down by a factor f_1, given by:

$$f_1 = \frac{\Delta r_A}{\Delta r_1}$$

where Δr_A is the displacement increment that ends at the next event. This ensures that a new equilibrium state is reached at the point A. The remainder of the load, $(1-f_1)\Delta R$, is then calculated and a new displacement increment, Δr_2, is found using stiffness K_2 (see Fig 2.6c). Again this displacement increment exceeds that required to reach the next event at B, so both it and the load increment are scaled by a factor f_2, given by:

$$f_2 = \frac{\Delta r_B}{\Delta r_2}$$

where Δr_B is the displacement increment that ends at event B. So once again the solution is in equilibrium. The remainder of the load, $(1-f_1)(1-f_2)\Delta R$ is then calculated and a new displacement increment, Δr_3, is found using stiffness K_3 (see Fig 2.6d). This time the increment is less than that required to reach the next event and the factor, f_3 is set to one. The element is now sustaining the load, $R_o + \Delta R$, and has not deviated from the equilibrium path in order to reach this final equilibrium state. When an element unloads the event factor is set to zero to ensure that the stiffness is updated immediately. It should also be noted that event factors can be determined using forces instead of displacements.

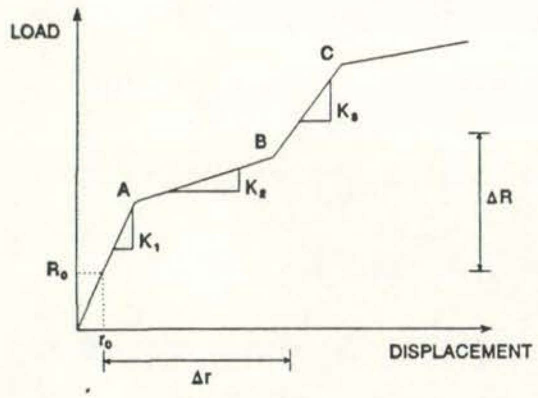

Fig. 2.6a Load Displacement Relationship

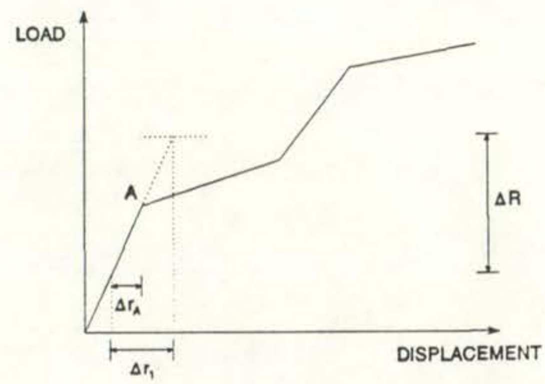

Fig. 2.6b First Event

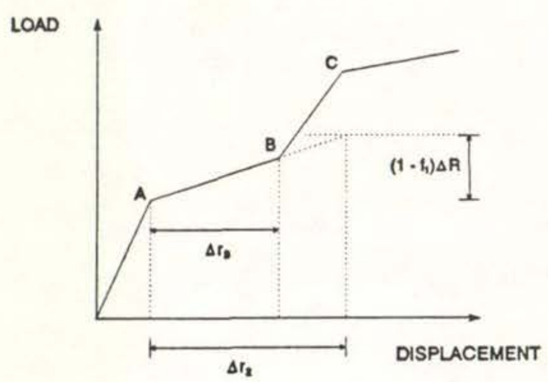

Fig. 2.6c Second Event

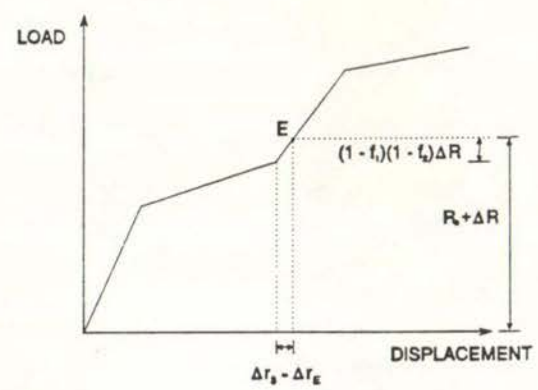

Fig. 2.6d End of Step

If elements have curvilinear action-deformation relationships, the event definition is chosen so that the solution remains close to the exact path and the errors that result at the end of the load step are applied as a correction in the next step. For structures with more than one element, event factor calculations are carried out on all the nonlinear elements, and the loads and displacements are scaled by the smallest event factor. The static analysis terminates when a specified maximum load, displacement, or number of load steps is reached.

Dynamic Analyses Procedure

For dynamic analyses DRAIN-2DX uses a similar 'event-to-event' procedure to that used for the static analyses, but it includes corrections to ensure that energy balance and equilibrium are satisfied at the end of each load step. The Constant Average Acceleration step-by-step method is used to perform all integration calculations. It is followed by velocity and acceleration modification procedures to correct the energy balance and satisfy equilibrium respectively. To minimise the discretization errors that are introduced when a dynamic problem is solved by a step-by-step integration method, DRAIN-2DX provides an automatic time step function. This function basically ensures a specified level of accuracy for the solution by using either a measure of the mean equilibrium error or the equivalent impulse error for each step in order to provide a basis for automatically selecting the integration time step. In this way a compromise is reached between the accuracy of the solution obtained by selecting very small time steps and the computational costs which increase with the number of steps employed.

DRAIN-2DX was used to perform all the analyses carried out in this report.

Further details about the solution strategies and procedures employed by DRAIN-2DX can be obtained from Reference [4].

2.2.3 Structure of the Hinge Model

The structure shown in Fig. 2.7 was devised to model the behaviour of the plastic hinge zones. It consists of a steel and concrete truss type element placed at the centroids of the top and bottom steel of the section, a flexural beam type element, and four rigid beam elements.

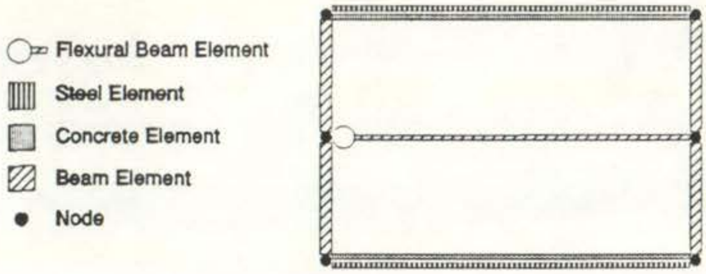

Fig. 2.7 The Hinge Structure

The flexural beam type element is given a very large shear stiffness so that it carries the shear force, but has a very small flexural stiffness and a release at one end to ensure that it transfers negligible axial loads and no bending moments. The release is incorporated into the element by giving it a flexural stiffness equivalent to:

$$K = \frac{EI}{L}\begin{bmatrix} 0 & 0 \\ 0 & 3 \end{bmatrix}$$

The four vertical elements are essentially rigid beam elements. The length of the 'structure' is small: typically one fifteenth of the depth of the member. This enables the central shear carrying element to be very stiff and so ensures there is only a very small shear deflection across the hinge zone. The steel and concrete elements are new truss elements designed specifically to model the concrete and steel within the hinge zones and are accordingly assigned properties to represent the actual reinforced concrete within these areas. In order to derive realistic concrete and steel strain values the length of these truss elements can be artificially scaled to a value more representative of the actual plastic hinge length. Assembling the elements in this way and giving them these properties ensures that the elongation of the member will only result from the flexural deformation properties of the steel and concrete elements.

2.2.4 The Plastic Hinge Steel Element

The elongation of reinforced concrete beams has been shown to be directly related to the yielding behaviour of the reinforcement in the plastic hinge zones of the member.

It is therefore important to produce an element which models the yielding properties of the reinforcement with some degree of accuracy.

The monotonic behaviour of steel is well known (see Fig. 2.8). The initial stress-strain relationship is linear with an elastic modulus of around 200 GPa, until the proportionality limit is reached, (point A). At this point the stress-strain relationship differs slightly depending on whether the reinforcing bar is machined or not.

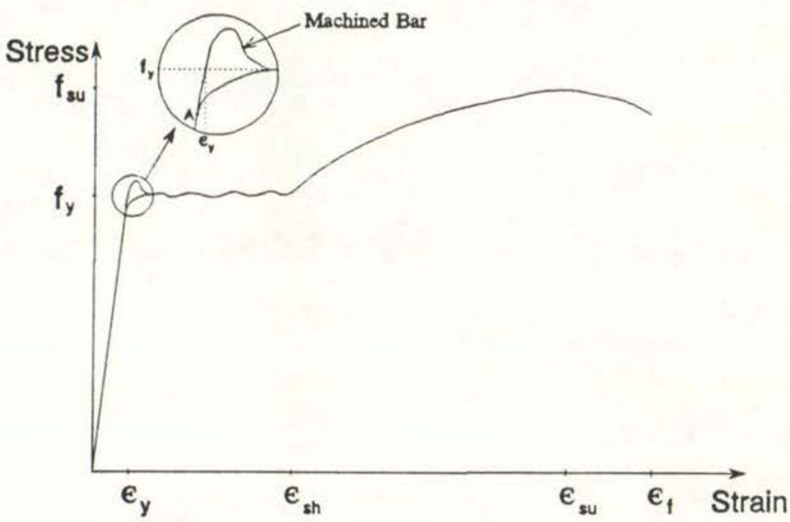

Fig. 2.8 Steel Monotonic Stress-Strain Curve

Once the bar has yielded it reaches a yield plateau region, where the stress remains constant (at the yield value) until the onset of strain hardening. The stress then increases until an ultimate stress value is reached. Once this value is exceeded the stress decreases until fracture occurs. The inelastic cyclic behaviour of reinforcement is perhaps not quite so well known, but there is an accepted stress-strain relationship [5]. For the first half cycle of cyclic loading, the stress-strain pattern is the same as that for the monotonic loading case. However, once the yield value has been exceeded, if the load reverses a nonlinear stress-strain relationship develops where there is no definite yield point (see Fig 2.9). This is referred to as the Bauschinger effect. Every new half cycle of loading is dependent upon the previous strain history of the steel.

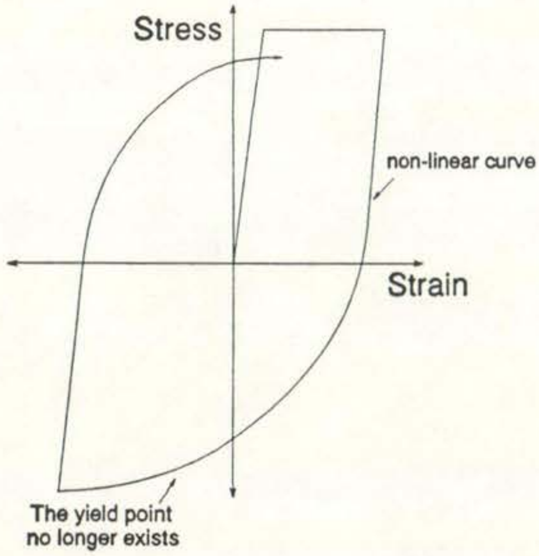

Fig. 2.9 Steel Cyclic Stress-Strain Curve

Many researchers have developed equations to describe the stress-strain characteristics of steel. After comparing a number of these methods with experimental results, Tjokrodimuljo [5] concluded that with some modifications a model developed by Menegotto and Pinto [6] was probably the most accurate and was relatively simple. As a result it was decided to use this modified method to describe the stress-strain characteristics of the new steel element. The complete modified model, as given by Trokrodimuljo [5], is summarised below and in Figs. 2.10 and 2.11.

The Improved Menegotto and Pinto Method.

(1) For the initial cyclic loading in the elastic range:

$$f = E_s \cdot \varepsilon \qquad (2.4)$$

where:

f, ε = stress and strain of steel at any point on the curve respectively

E_s = elastic modulus of steel

(2) For the curve where the yield strain is exceeded for the first time:

$$f = E_s\, \varepsilon_y \qquad \text{for } \varepsilon < \varepsilon_y \tag{2.5}$$

$$f = f_y \qquad \text{for } \varepsilon_y < \varepsilon_y \leq \varepsilon_{sh} \tag{2.6}$$

$$f = p\, f_y \qquad \text{for } \varepsilon_{sh} < \varepsilon_y \leq \varepsilon_{su} \tag{2.7}$$

where:

$$p = \frac{m(\varepsilon - \varepsilon_{sh}) + 2}{60(\varepsilon - \varepsilon_{sh}) + 2} + \frac{(\varepsilon - \varepsilon_{sh})\,(60 - m)}{2(30q + 1)^2}$$

$$m = \frac{(f_{su}/f_y)\,(30q + 1)^2 - 60q - 1}{15\, q^2}$$

$$q = \varepsilon_{su} - \varepsilon_{sh}$$

f_y = yield stress of the steel

f_{su} = ultimate stress of the steel

ε_y = yield strain of the steel

ε_{sh} = strain at the starting point of strain hardening

ε_{su} = strain at the ultimate stress

(3) For the curves after the yield strain has been exceeded:

$$0 \quad f^* = b\, \varepsilon^* + \frac{(1 - b)\, \varepsilon^*}{\left(1 + \varepsilon^{*R}\right)^{1/R}} \tag{2.8}$$

where:

$$\varepsilon^* = (\varepsilon - \varepsilon_1) \,/\, (\varepsilon_o - \varepsilon_1)$$

$$f^* = (f - f_1) \,/\, (f_o - f_1)$$

$$b = E_b \,/ E_s$$

$$R = Y \; \log_e \varepsilon_{rev}$$

$$Y = 0.40 + 3.6\, X^{-0.9}$$

$$X = (\log_e \varepsilon_{rev})^2 \left\{\log_e (\varepsilon_{sht} + 20) - 2\right\}$$

$$\varepsilon_{rev} = \varepsilon_{amp} / \varepsilon_y$$

$$\varepsilon_{sht} = \frac{\sum \varepsilon_{asc} - 0.925 \sum \varepsilon_{des}}{\varepsilon_y}$$

$f_o = E_s\, \varepsilon_o + (f_1 - E_s\, \varepsilon_1)$, stress at the intersection between two asymptotes

$\varepsilon_o = \dfrac{f_{or} - f_1 + E_s\, \varepsilon_1 - E_b\, \varepsilon_{or}}{E_s - E_b}$, strain at the intersection between two asymptotes

$E_b = \dfrac{f_{0.06} - f_y}{0.06 - \varepsilon_y}$, is the gradient of the second asymptote

E_s = elastic modulus of the steel

ε_1 , f_1 = strain, stress at the starting point of the curve

f_{or} = stress at the origin of the second asymptote

where:

$f_{or} = f_y$, for ascending curve, and

$f_{or} = - n\, f_y$, for descending curve

ε_{or} = strain at the origin of the second asymptote

where:

$\varepsilon_{or} = \varepsilon_1 + \dfrac{f_{or} - f_1}{E_s}$, but will be;

$\varepsilon_{or} = \varepsilon_y$, if $\varepsilon_1 + \dfrac{f_{or} - f_1}{E_s} > \varepsilon_y$ for ascending curve , and

$\varepsilon_{or} = - n\, \varepsilon_y$, if $\varepsilon_1 + \dfrac{f_{or} - f_1}{E_s} < - n\, \varepsilon_y$ for descending curve

n = a parameter which is influenced by the inelastic buckling conditions of the steel under compressive loading (i.e. the ratio of the spacing of the buckling protection and the diameter of the steel): n = 1.0 for a machined bar specimen which does not undergo inelastic buckling under compressive loading, and n = 1.1 for reinforcing steel which may be subjected to inelastic buckling condition

$f_{0.06}$ = stress corresponding to strain 0.06 in the stress-strain curve of the steel under monotonic loading in tension

ε_{amp} = strain amplitude of the previous half cycle

$\Sigma\varepsilon_{asc}$ = total strain amplitude for all previous ascending curves after the yield strain has been exceeded

$\Sigma\varepsilon_{des}$ = total strain amplitude for all previous descending curves after the yield strain has been exceeded

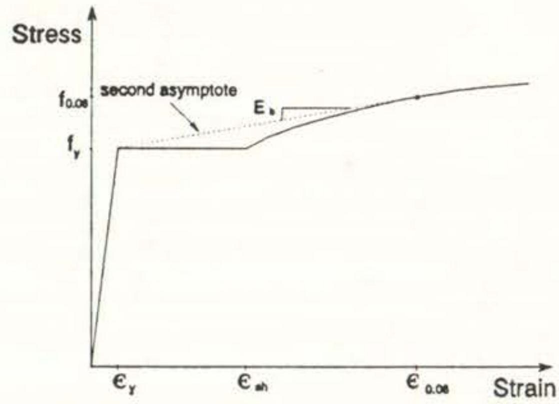

Fig. 2.10 Improved Menegotto and Pinto Method: Steel Monotonic Stress-Strain Curve

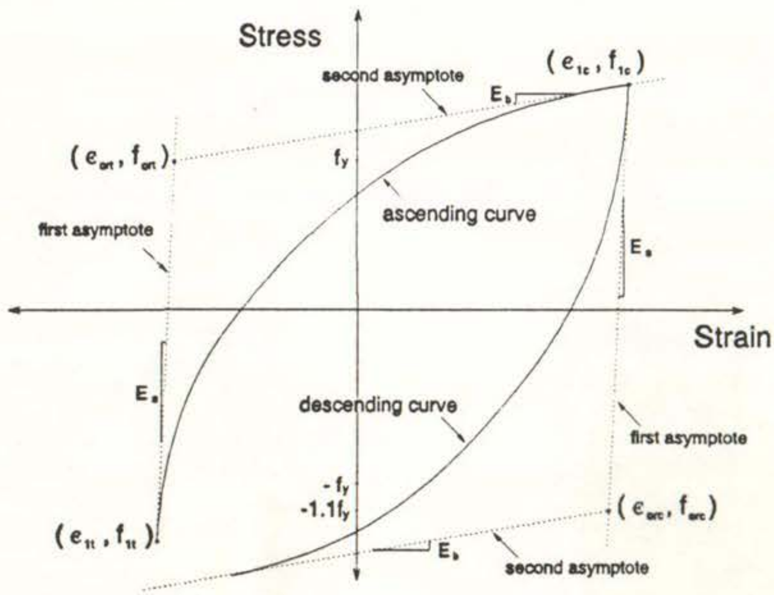

Fig. 2.11 Improved Menegotto and Pinto Method: Steel Cyclic Stress-Strain Curve

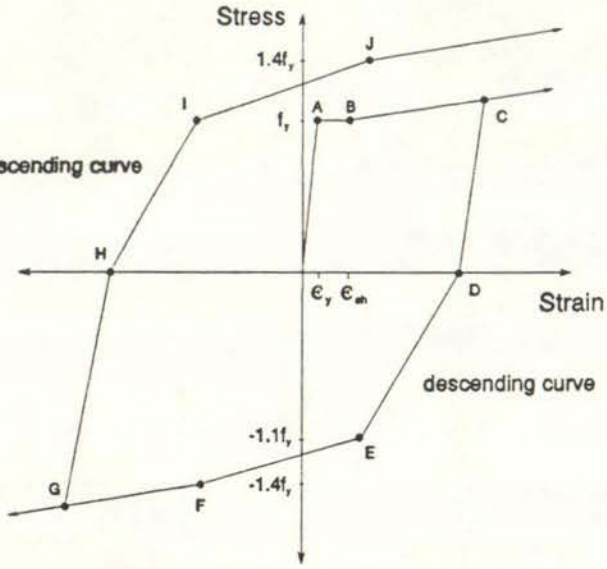

Fig. 2.12a Element Events

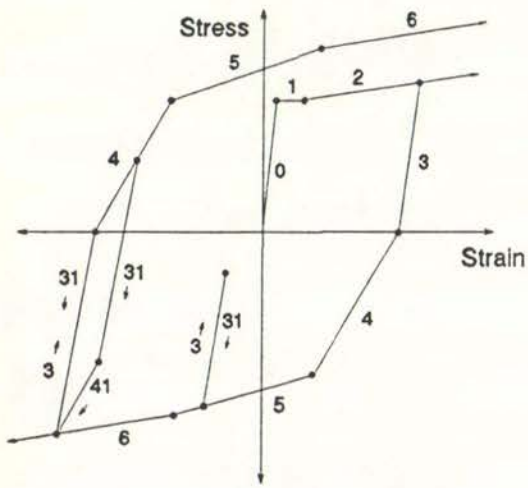

Fig. 2.12b Element Yield Codes

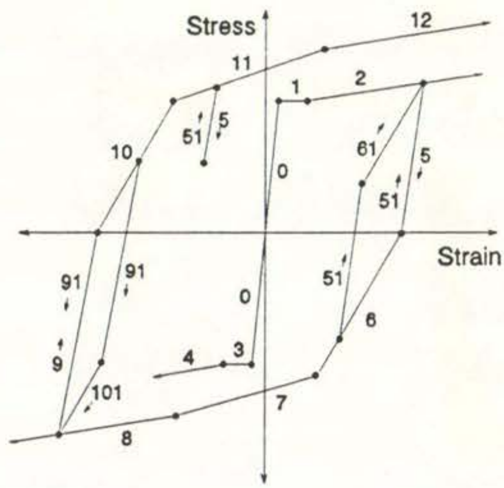

Fig.2.12c Element Event Codes

Because of the nature of the event-to-event solution scheme employed by DRAIN-2DX, it was necessary to define 'events' at different intervals along the unloading and reloading curves and then to redefine the curves as the set of lines that joined these points. To ensure that the solution remained close to the improved Menegotto and Pinto hysteresis path the events are defined in terms of fixed stress values (points; A, B, D, E, F, H, I and J) as shown in Fig. 2.12a. The associated event strains are then calculated from Trokrodimuljo's [5] improved Menegotto and Pinto equations using Newton-Raphson iterations. The yield and event codes that are used to describe the state of the steel element, with respect to its position on the hysteresis loop, can be seen in Figs. 2.12b and 2.12c respectively.

The aim of the Newton-Raphson scheme for this problem is to find a value for the strain at the next event such that;

$$u = f(\varepsilon^{*}) - f_{evt} = 0 \tag{2.9}$$

where:

$$f(\varepsilon^{*}) = \left(\frac{b\,\varepsilon^{*} + (1 - b)\,\varepsilon^{*}}{\left(1 + \varepsilon^{*R}\right)^{\frac{1}{R}}} \right) (f_o - f_1) + f_1$$

To do this, a number of iterations are used to solve equation 2.10 until the desired convergence criteria are achieved and the value for the strain at the next event is obtained.

$$\varepsilon_{x+1} = \varepsilon_x - \frac{f(\varepsilon_x)}{f'(\varepsilon_x)} \tag{2.10}$$

where:

$f(\varepsilon_x)$ is obtained using equation 2.8, and

$$f'(\varepsilon_x) = \frac{\partial f}{\partial \varepsilon^{*}} \; \frac{\partial \varepsilon^{*}}{\partial \varepsilon}$$

$$= \left(\frac{b + (1 - b)}{\left(1 + \varepsilon^{*R}\right)^{\frac{1}{R}}} \left(1 - \frac{\varepsilon^{*R}}{\left(1 + \varepsilon^{*R}\right)} \right) \right) \left(\frac{f_o - f_1}{\varepsilon_o - \varepsilon_1} \right)$$

Once the stress and strain values at the next event are known, the stiffness gradient between the last and the next event can be determined and the force and deflection increments can then be calculated.

In order to employ the steel element in a structural analysis, the user need only input values for; the tensile and compressive yield stress, Young's Modulus, the member cross-sectional area, the strain at which strain hardening begins and a code value indicating whether or not the reinforcing bar is subject to inelastic buckling conditions.

2.2.5 The Plastic Hinge Concrete Element

One factor contributing to the elongation of reversing plastic hinges has been shown to be the wedging type actions that results from dislocated aggregate particles that become lodged within the cracks of reinforced concrete members during cyclic loading. Consequently it was necessary to develop a concrete element which effectively modelled this action.

A large number of methods for predicting the stress-strain behaviour of concrete under inelastic cyclic conditions have been developed, but in most of these the stress carrying capacity of the concrete has been neglected in the tensile region, particularly after cracks have been assumed to form. Research carried out by Bolong et.al. [7] into the effects of opening and closing cracks, suggests that the compression carrying capacity of concrete in the tensile strain region can be quite significant, even when cracks in the concrete are still evident. They discovered that during reloading, as a concrete crack closes it starts to carry a small proportion of the compression force by transmitting the local pressures within the crack. As the level of closure increases, so too does the 'contact' compression force. Bolong et.al. have developed a number of equations to represent the stress-strain characteristics of concrete under cyclic loading which include these contact effects. These equations are given below and illustrated in Fig. 2.13.

Bolong et.al. Method.

(1) The monotonic stress-strain curve:

$$f = \left(2\, f_c' \,\varepsilon\right) / \left(\varepsilon_o + \varepsilon\right) \qquad \text{for } \varepsilon \le \varepsilon_o \qquad (2.11)$$

$$f = f_c' \left\{1 - \left[200\left(\varepsilon - \varepsilon_o\right)\right]^2\right\} \qquad \text{for } \varepsilon_o \le \varepsilon \le \varepsilon_a \qquad (2.12)$$

$$f = 0.3\, f_c' \qquad \text{for } \varepsilon_a \le \varepsilon \qquad (2.13)$$

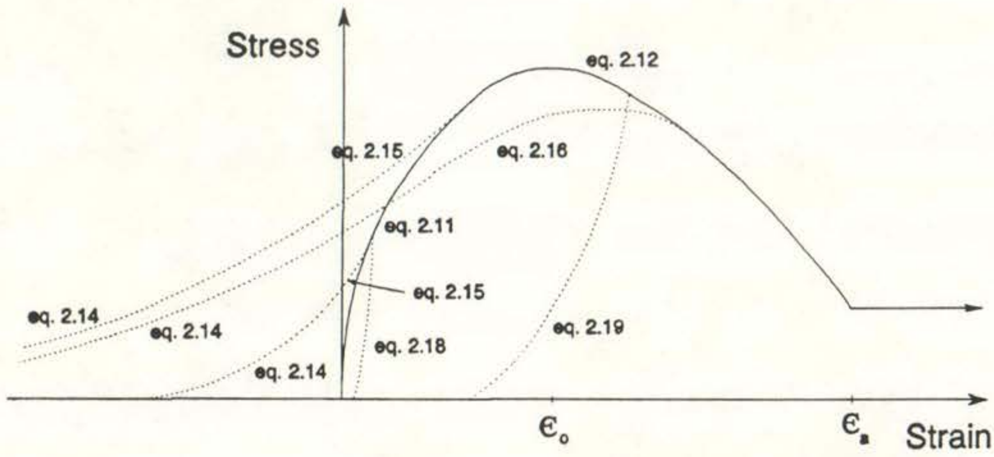

Fig. 2.13 Stress-Strain Concrete Curve under Cyclic Loading Proposed by Bolong et al.

(2) The stress-strain curve under cyclic loading:

(a) Reloading Curves

$$f = f_{co}\left(1 - \frac{2\,\varepsilon}{\varepsilon_{cs} + \varepsilon}\right) \qquad \text{for } \varepsilon_{min} < \varepsilon < 0 \qquad (2.14)$$

$$f = f_{co}\left(1 - \frac{\varepsilon}{\varepsilon_o}\right) + \left(\frac{2\,\varepsilon}{\varepsilon_o + \varepsilon}\right) f_c' \quad \text{for } 0 \le \varepsilon\,,\ \ \varepsilon_{max} < \varepsilon_o\,,\ \ \varepsilon_{min} < 0 \qquad (2.15)$$

$$f = f_c'\left(1 - \frac{\varepsilon}{\varepsilon_{max}}\right) + \left(\frac{2\,\varepsilon}{\varepsilon_{max} + \varepsilon}\right)\left(\frac{2\,\varepsilon_o}{\varepsilon_{max} + \varepsilon_o}\right) f_{max}$$

$$\text{for } 0 \le \varepsilon\,,\ \ \varepsilon_o < \varepsilon_{max} \qquad (2.16)$$

$$f = 2\,f_c'\left(\frac{\varepsilon - 0.2\,\varepsilon_{max}}{\varepsilon_o + \varepsilon - 0.2\,\varepsilon_{max}}\right) \qquad \text{for } \varepsilon_{min} > 0 \qquad (2.17)$$

(b) Unloading curves:

$$f = \frac{(\varepsilon - 0.2\ \varepsilon_{max})\ f_{max}}{1.8\ \varepsilon_{max} - \varepsilon} \qquad \text{for} \quad \varepsilon_{max} \leq \varepsilon_o \tag{2.18}$$

$$f = \frac{(2\ \varepsilon - \varepsilon_{max})\ f_{max}}{3\ \varepsilon_{max} - 2\ \varepsilon} \qquad \text{for} \quad \varepsilon_o \leq \varepsilon_{max} \tag{2.19}$$

where:

$$\varepsilon_{cs} = \varepsilon_{min} \left(0.1 + \frac{0.9\ \varepsilon}{\varepsilon_o + \varepsilon_{min}} \right) \tag{2.20}$$

is the strain where contact effects start

ε_{min} = the minimum strain where the repeated loading starts

ε_{max}, f_{max} = the strain and stress at the starting point of the previous unloading curve

$$f_{co} = 0.3\ f_c' \left[2 + \frac{(\varepsilon_{cs} / \varepsilon_o) - 4}{(\varepsilon_{cs} / \varepsilon_o) + 2} \right] \tag{2.21}$$

is the stress when $\varepsilon = 0$, in the reloading curve

Work carried out by Tjokrodimuljo [5] at Auckland University led to a modification of Bolong et al's equation for the strain at which contact effects begin. This is given in equation 2.22.

$$\varepsilon = 0.8\ \varepsilon_o \left(\frac{\varepsilon_{max}}{\varepsilon_o} - 1 \right) \tag{2.22}$$

where ε_o is assumed to be 0.002 and ε_{max} is the strain at the starting point of the previous unloading curve. With this modification Bolong et al's equations were shown to model concrete stress-strain experimental hysteretic curves adequately [5].

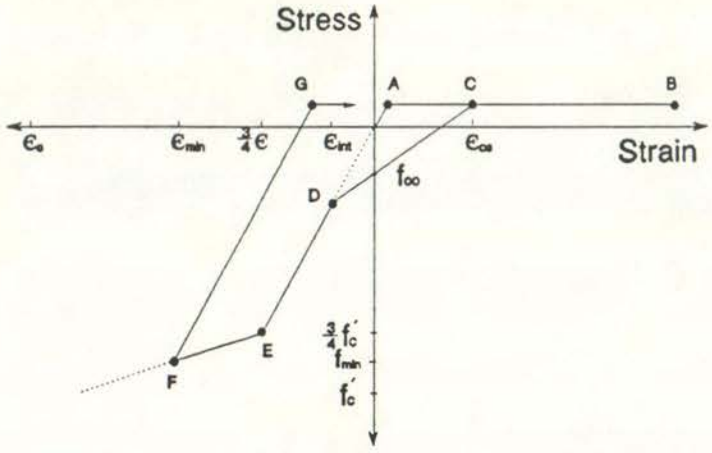

Fig. 2.14a Plastic hinge Concrete Hysteresis Loop and Element Events

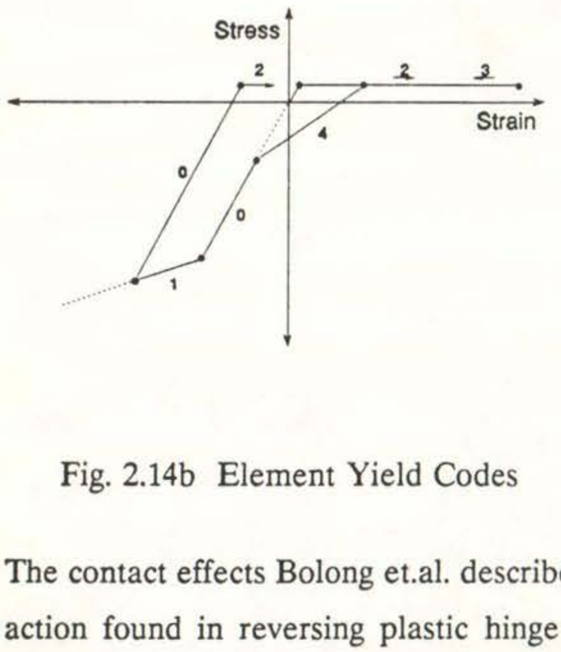

Fig. 2.14b Element Yield Codes

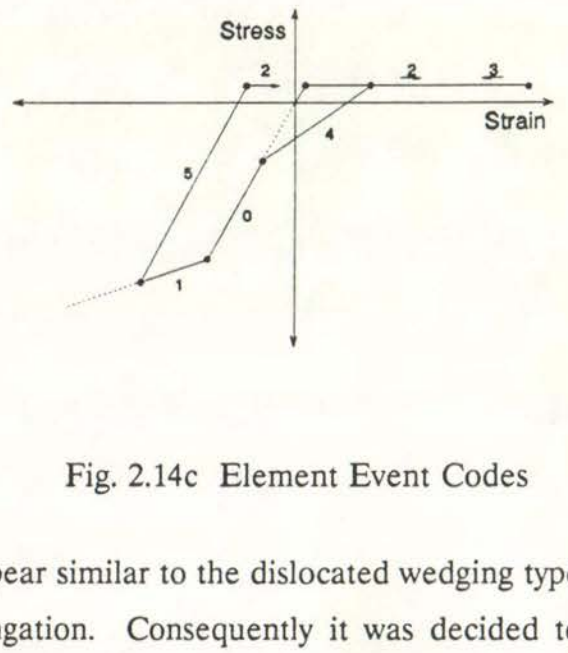

Fig. 2.14c Element Event Codes

The contact effects Bolong et.al. describe appear similar to the dislocated wedging type action found in reversing plastic hinge elongation. Consequently it was decided to employ the improved contact effect equations in a simplified model to represent the stress-strain characteristics of plastic hinge zone concrete. The equations and the events employed to describe this relationship are given below and illustrated in Fig. 2.14a (points A to G). The yield and event code values used to describe the state of the concrete element with respect to its position on the hysteresis loop can be seen in Figs. 2.14b and 2.14c respectively.

For decreasing strains:

$$f = f_{cr} + E_c \varepsilon \qquad \text{for } \varepsilon_{3/4} < \varepsilon < \min(\varepsilon_{cr}, \varepsilon_{int}) \qquad (2.23)$$

$$f = \tfrac{3}{4} f_c' + psh\, E_c\, \varepsilon \qquad \text{for } \varepsilon_o < \varepsilon < \varepsilon_{3/4} \qquad (2.24)$$

$$f = f_{max} + 0.0001\, E_c(\varepsilon - \varepsilon_{max}) \qquad \text{for } \varepsilon_{cs} < \varepsilon \le \varepsilon_{max} \qquad (2.25)$$

$$f = f_{co} + E_{cs}\, \varepsilon \qquad \text{for } \varepsilon_{int} < \varepsilon \le \varepsilon_{cs} \qquad (2.26)$$

For increasing strains:

$$f = f_{min} + E_c\,(\varepsilon - \varepsilon_{min}) \qquad \text{for } \varepsilon_{min} < \varepsilon < \varepsilon_{cr} \qquad (2.27)$$

$$f = f_{cr} + 0.0001\, E_c\,(\varepsilon - \varepsilon_{cr}) \qquad \text{for } \varepsilon_{cr} \le \varepsilon \qquad (2.28)$$

where

f_{cr} = tensile stress at which concrete cracks

$\varepsilon_{cr} = \varepsilon_{min} + \dfrac{f_{cr}}{E_c}$, strain at which concrete cracks

E_c = concrete modulus

$\varepsilon_{3/4} = \varepsilon_{cr} + \dfrac{-\tfrac{3}{4} f_c'}{E_c}$

$psh = \left(\dfrac{f_c' - \tfrac{3}{4} f_c'}{\varepsilon_o - \varepsilon_{3/4}}\right)$, concrete pseudo strain-hardening factor

$\varepsilon_{max}, f_{max}$ = maximum strain, stress values from the tensile loading

$\varepsilon_{min}, f_{min}$ = minimum strain, stress values from the previous compression loading

$E_{cs} = \left(\dfrac{f_{co} - f_{cs}}{-\varepsilon_{cs}}\right)$, contact stress modulus

$f_{co} = -0.3 f_c' \left[2 + \dfrac{(\varepsilon_{cs}/\varepsilon_o) - 4}{(\varepsilon_{cs}/\varepsilon_o) + 2}\right]$, contact stress at zero strain

$f_{yo} = f_{min} - \varepsilon_{min} E_c$

$\varepsilon_{cs} = 0.8\, \varepsilon_o \left(\dfrac{\varepsilon_{min}}{\varepsilon_o} - 1\right)$, strain at which contact stresses start

$\varepsilon_{int} = \dfrac{(f_{co} - f_{yo})}{(E_s - E_{cs})}$, strain intercept value.

To employ the concrete element in a structural analysis the user need only input values for; tensile cracking and compressive yielding, the cross-sectional area of the member and a code indicating whether or not contact effects are to be taken into consideration.

Chapter 3

PROGRAMMING VERIFICATION

3.1 Introduction

A number of cyclic analytic tests were performed on the new steel and concrete elements to ascertain the accuracy of their respective programme coding. The composite hinge structure was also tested to verify the adequacy of its element configuration for modelling the flexural characteristics of plastic hinges. Descriptions of these tests and their results are contained within this chapter.

It is important to note that the 'events' that occur during the loading sequences cause more dramatic load-deformation patterns than would normally be expected, because of the linear nature of the hysteresis loops employed to describe the behaviour of the elements.

3.2 Testing of the Steel Element

The test system shown in Fig. 3.1 was used to assess the reaction of the steel element to a series of cyclic static load tests.

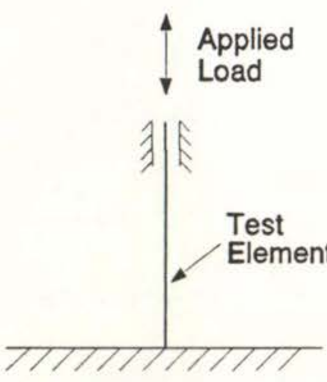

Fig. 3.1 Element Test System

The element was assigned a unit length so that resulting extensions were equivalent to element strains and typical steel properties were chosen to describe its stress-strain characteristics (see Table 3.1).

Table 3.1 Test Steel Element Properties

Steel Properties	Values
Young's Modulus, E	200 GPa
Cross-Sectional Area, A	$0.001 m^2$
Length	1m
Yield Stress	430 MPa
Strain at start of start hardening, ε_{sh}	0.003
Strain at ultimate stress, ε_{su}	0.25
Ultimate stress, f_{su}	650 MPa
Inelastic buckling condition parameter for compressive loading, rn	
- For machined bar which does not undergo inelastic buckling under compressive loading, rn = 1.0	1.1
- For reinforcing steel which may be subjected to inelastic buckling conditions, rn = 1.1	

The resulting element force-extension curves from three of these static tests are illustrated in Figs. 3.2, 3.3 and 3.4. As can be seen from the figures the hysteresis loops generated follow the accepted steel force-extension relationship (see Fig. 2.9) given the linear nature of the solution scheme. The monotonic curve is traced for the first half cycle and the Bauschinger effect and its associated stiffness degradation and strain hardening are incorporated into the remaining cyclic load pattern.

Due to the large extensions resulting from all three tests, the yield plateau region of the monotonic curve is comparatively very small and consequently hard to distinguish in any of the figures. However from the yield codes and the force and extension values obtained from the tests, it is clear that the steel element yields at the expected force of 430 kN and that the yield plateau region does exist before strain hardening begins at the

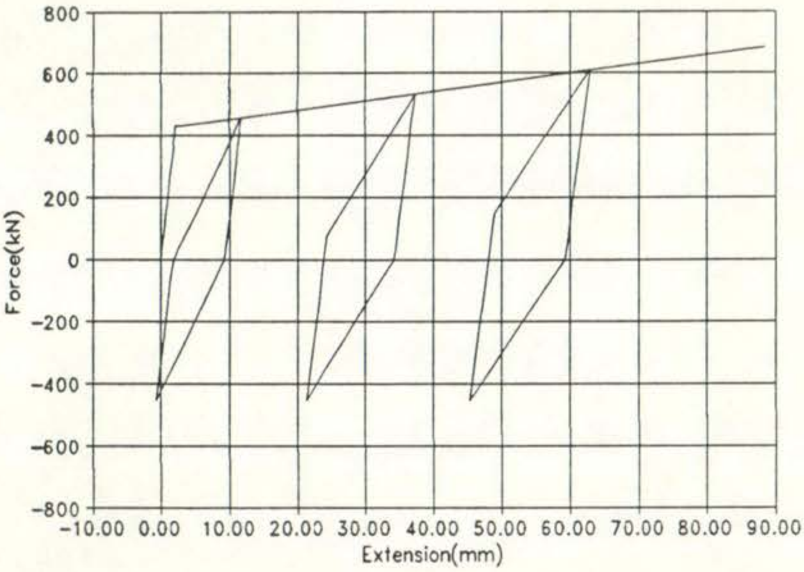

Fig. 3.2 Steel Force versus Extension Hysteresis Loops - Demonstrating post yield elastic loading cycles

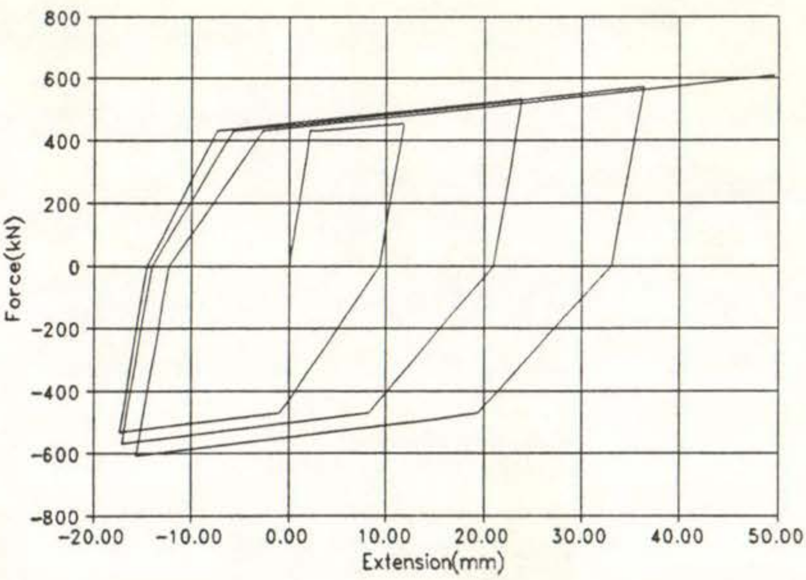

Fig. 3.3 Steel Force versus Extension Hysteresis Loops - Demonstrating inelastic loading cycles

desired strain value. In Fig. 3.2 the descending curves all remain within the elastic range and no negative yielding occurs, but in Fig. 3.3 both ascending and descending curves

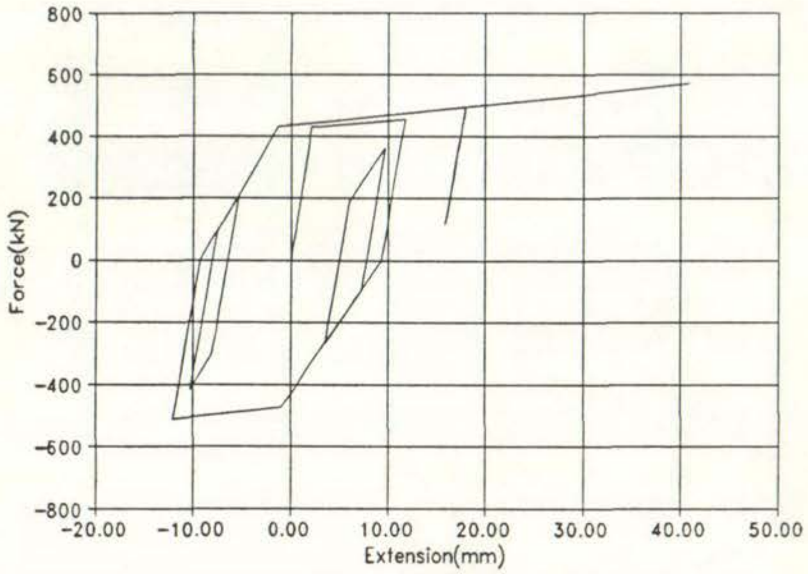

Fig. 3.4 Steel Force versus Extension Hysteresis Loops - Demonstrating a combination of elastic and inelastic loading cycles

have inelastic deformations. The steel hysteresis loop shown in Fig. 3.4 illustrates a combination of both elastic and inelastic loading cycles, confirming the ability of the programme code to cope with varied loading sequences. It is evident from all three graphs that the force-extension values obtained are an acceptable representation of the experimental results that would be expected from similar loading patterns.

3.3 Testing of the Concrete Element

The test system illustrated in Fig. 3.1 was also used to assess the behaviour of the concrete element under a series of cyclic static load tests. Once again the element was assigned a unit length and given typical concrete properties to describe its stress-strain characteristics (see Table 3.2). The force-extension graphs from three of these load sequences are illustrated in Figs. 3.5, 3.6 and 3.7.

Table 3.2 Test Concrete Element Properties

Concrete Properties	Values
Concrete Modulus, E_c	29.35 MPa
Cross-Sectional Area, A	$0.1m^2$
Length, l	1m
Post Crack Stress, f_{yp}	5 MPa
Cylinder Compressive Stress, f_c'	44.9 MPa
Contact Stress Code - 0: ignore contact stress effects - 1: include contact stress effects	1

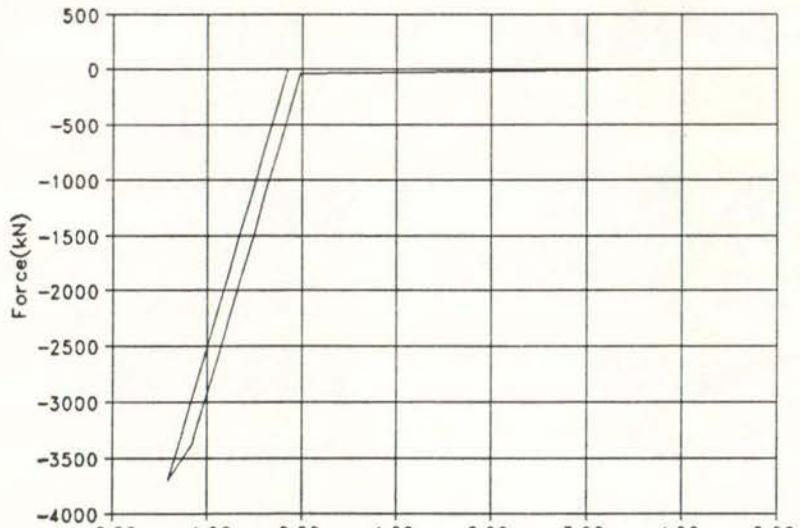

Fig. 3.5 Concrete Force versus Extension Hysteresis Loop Excluding Contact Stress Effects

Fig 3.5 shows a typical concrete force-extension loop for the case when contact effects are ignored. The concrete element is taken through a 'compression-tension-compression'

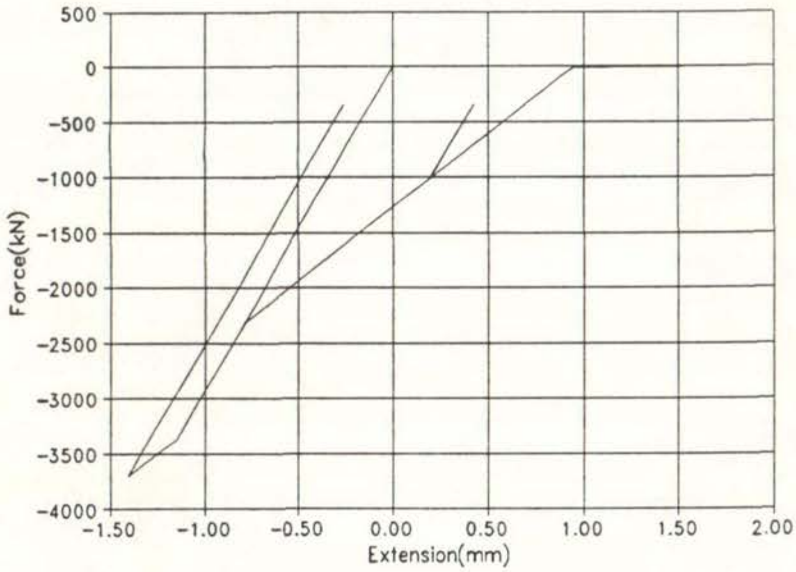

Fig. 3.6 Concrete Force versus Extension Hysteresis Loop Including Contact Stress Effects

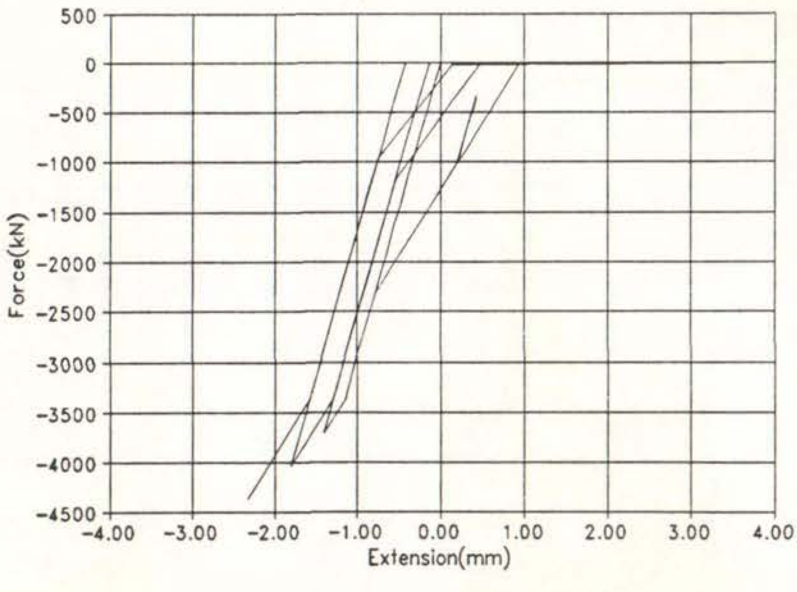

Fig. 3.7 Concrete Force versus Extension Hysteresis Loops Including Contact Stress Effects: Demonstrating multiple loading cycles

loading cycle. As can be seen from the graph the concrete does not sustain any compression load until the 'cracks' in the element are completely closed, that is, until the element starts compressing. Figs. 3.6 and 3.7 illustrate the hysteresis loop generated when contact effects are included. From both graphs it is clear that the concrete element starts sustaining compression forces when it is still effectively 'cracked', thus representing the wedging type action of the aggregate particles. Fig. 3.7 confirms the ability of the programme code to cope with multiple 'yield-crack-yield' sequences. As can be seen from all three figures the force-extension magnitudes obtained are within acceptable bounds for concrete and the patterns of the hysteresis loops are as expected allowing for the linear nature of the solution scheme (see Fig. 2.13).

3.4 Testing of the Hinge Structure

The single hinge testing system shown in Fig. 3.8 was set up to verify the ability of the chosen hinge structure to adequately model the mechanics of plastic hinge elongation.

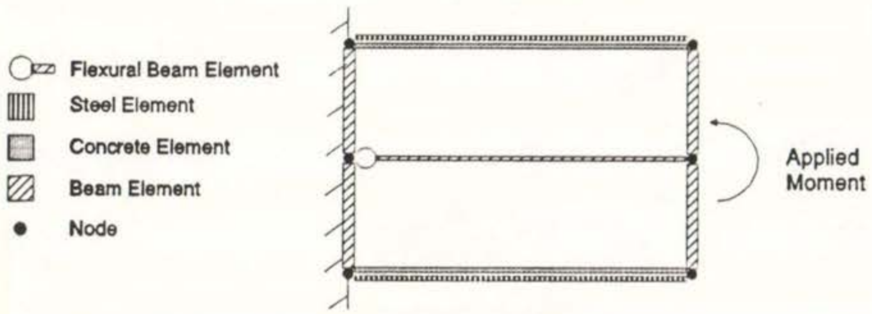

Fig. 3.8 Hinge Model Testing System

An anti-clockwise moment was applied as shown, then taken through two complete load reversals. Table 3.3 is a time-table of the events that occurred during the load reversals. Most of the events occur when the elements are in tension, although the steel elements do yield in compression before the 'cracks' in the corresponding concrete elements close enough to begin carrying a compressive load. As is evident from the table the chronological order in which the element events take place, is as expected for the applied loading sequence.

Table 3.3 Time-table of Test Hinge Element Events

Step No.	Event No.	Event Type	Event Factor	Group No.	Elem No.	Event Code	Load Factor	Event Description
1	1	1	0.001	2	2	2	0.000984	Bottom concrete cracks in tension: A
1	2	2	0.099				0.1	
2	1	2	0.1				0.2	
3	1	2	0.1				0.3	
4	1	2	0.1				0.4	
5	1	2	0.1				0.5	
6	1	2	0.1				0.6	
7	1	2	0.1				0.7	
8	1	1	0.0509	1	2	1	0.75094	Bottom steel reaches tension yield: B
8	2	1	0.0008	1	2	2	0.75169	Bottom steel starts strain-hardening
8	3	2	0.0483				0.8	
9	1	2	0.1				0.9	
10	1	5	0.1				1	C
1	1	1	0	1	1	1	0.000001	Top steel unloading from compression
1	2	2	0.1				0.1	
2	1	2	0.1				0.2	
3	1	2	0.1				0.3	
4	1	2	0.1				0.4	
5	1	1	0.065	1	2	6	0.46501	Bottom steel loading in compression: D
5	2	2	0.035				0.5	
6	1	1	0.0005	2	1	2	0.50049	Top concrete cracks in tension
6	2	2	0.0995				0.6	
7	1	2	0.1				0.7	
8	1	2	0.1				0.8	
9	1	1	0.0755	1	1	1	0.87547	Top steel reaches tension yield: E
9	2	1	0.0004	1	1	2	0.87585	Top steel begins strain-hardening
9	3	1	0.0067	1	2	7	0.88252	Bot. steel reaches first cyclic yield: $-1.1f_y$: F
9	4	2	0.0175				0.9	
10	1	1	0.0963	2	2	0	0.99634	Bottom concrete compressive loading: G
10	2	5	0.0037				1	H
1	1	1	0	1	1	5	0.000001	Top steel starts unloading from tension
1	2	1	0.0039	2	2	2	0.003877	Bottom concrete cracks in tension
1	3	2	0.0961				0.1	
2	1	2	0.1				0.2	
3	1	2	0.1				0.3	
4	1	2	0.1				0.4	
5	1	1	0.065	1	1	6	0.46501	Top steel sustains compressive load: I
5	2	2	0.035				0.5	
6	1	1	0.0013	1	2	10	0.50132	Bottom steel sustaining tensile load
6	2	2	0.0987				0.6	
7	1	2	0.1				0.7	
8	1	2	0.1				0.8	
9	1	1	0.0798	1	2	11	0.87977	Bottom steel reaches first cyclic yield: f_y: J
9	2	1	0.0027	1	1	7	0.88252	Top steel reaches first cyclic yield: $-1.1f_y$: K
9	3	2	0.0175				0.9	
10	1	1	0.0948	2	1	4	0.99478	Top concrete starts contact stress loading: L
10	2	5	0.0052				1	

The points A to L, which refer to the element events (see Table 3.3), are shown on some of the subsequent figures.

A plot of the applied moment against the resulting rotation of the hinge structure is illustrated in Fig. 3.9.

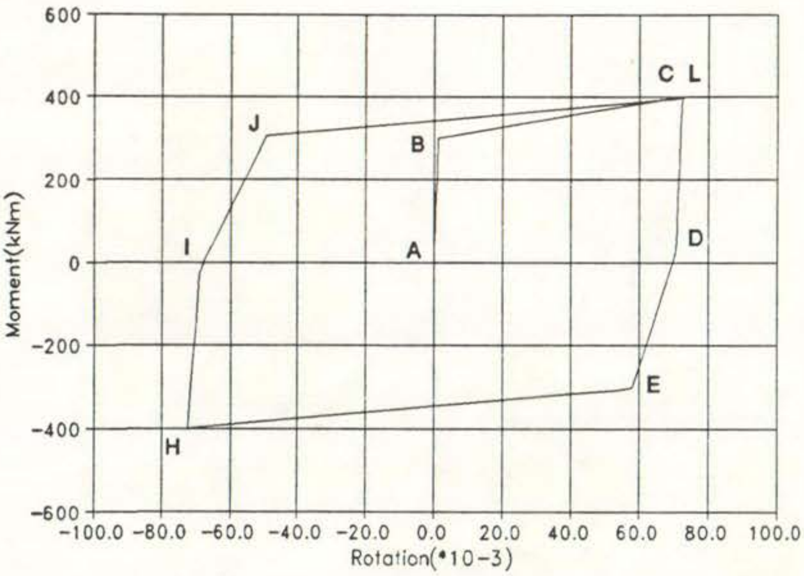

Fig. 3.9 Test Hinge Applied Moment versus Rotation Graph

Comparing this figure with the steel and concrete force-elongation loops illustrated in Figs. 3.10 and 3.11, it is clear that the steel behaviour dominates the moment-rotation reaction of the hinge structure, as it does in plastic hinge zones. Also the elongation of the hinge is primarily due to the yielding of the steel element which again, is as the theory suggests.

The applied moment-elongation graph shown in Fig. 3.12 requires a more indepth analysis to determine the validity of the mechanisms responsible for its irregular shape. The moment is initially applied anticlockwise. This puts the bottom concrete element in tension and causes it to 'crack' almost immediately. The remaining elements behave elastically from points A to B, with the majority of the compression loading being sustained by the top concrete element and virtually all of the tension load being carried

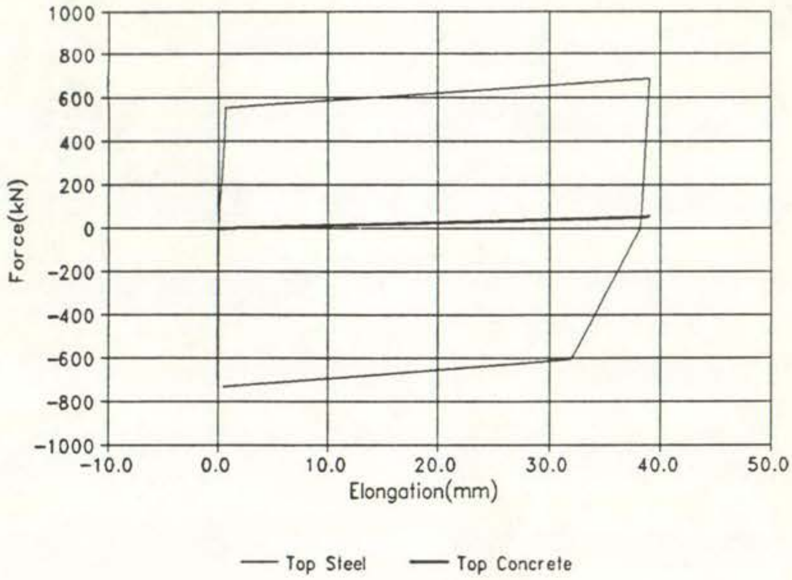

Fig. 3.10 Force versus Elongation Hysteresis Plots for the Top Steel and Concrete Elements of the Test Hinge

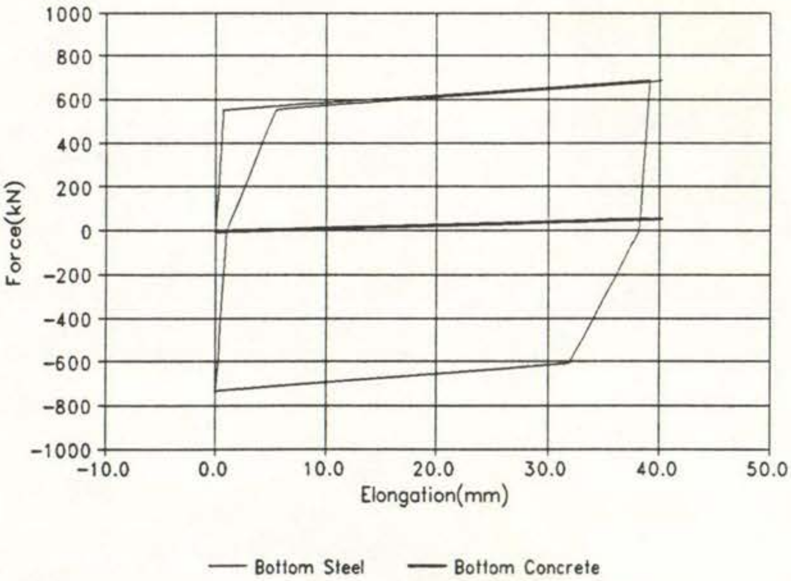

Fig. 3.11 Force versus Elongation Plots for the Bottom Steel and Concrete Elements of the Test Hinge

by the bottom steel element. At point B the bottom steel yields then begins strain-hardening to point C and is responsible for the rapid increase in the elongation of the

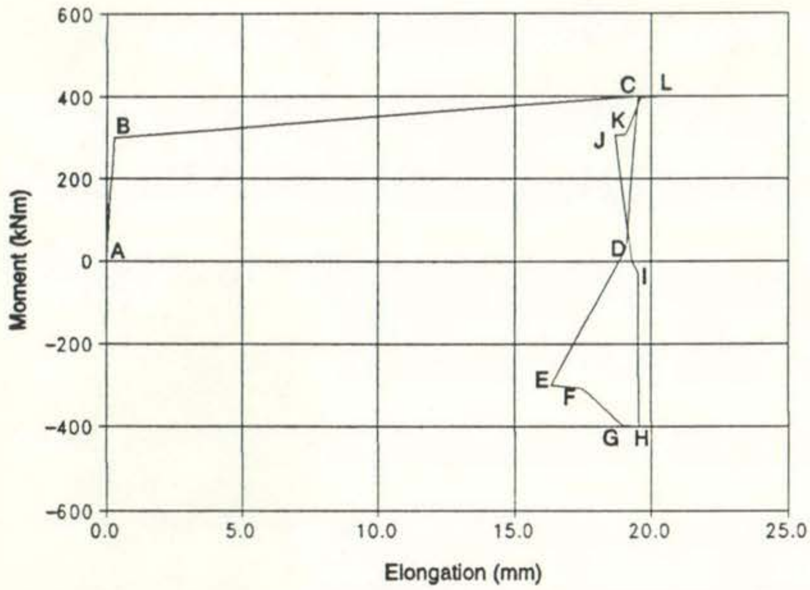

Fig. 3.12 Applied Moment versus Elongation Graph for the Test Hinge

hinge structure. At point C the moment is reversed and the loading on the elements begins to decrease. At point D the bottom steel begins to sustain compression forces which leads to a more rapid decrease in the overall elongation of the structure. This is due to the Bauschinger effect and the resulting stiffness degradation of the steel element. Soon after this the top concrete element goes into tension and cracks. At point E the top steel element yields in tension then begins strain hardening. This again causes the elongation of the hinge to increase significantly. However, the rate of this elongation nearly halves when the bottom compression steel begins yielding at point F. At this point both the top and bottom steel elements are yielding, but in opposite directions. At point G the cracks in the bottom concrete element close and it begins to sustain compressive loading. Consequently the elongation rate once again increases. Up to this point the bottom steel sustained all of the compression load. The moment is reversed for the final time at point H. Soon after, the bottom concrete element is loaded in tension and cracks. There is virtually no decrease in the elongation of the hinge structure however, until point I, at which the top steel begins to sustain a compressive load and there is a corresponding reduction in the element's stiffness, as with points D to E. At point J the bottom steel reaches tension yield for the second time, causing a large increase in the elongation of the hinge. At point K the top steel yields in compression, greatly reducing the rate of this increase. Finally, at point L, the top concrete element begins sustaining a compressive load resulting from contact effects and the elongation rate increases dramatically.

It is interesting to note that, although the pattern of events occurring between points C and H is practically the same as that from H to L (except that it is reversed), the reduction in the overall elongation of the hinge is less due to the stiffness degradation of the steel elements associated with the Bauschinger effect. Also although there has been a complete load reversal from C to H the elongation of the hinge has remained virtually unchanged. As can be seen from all the figures, the events that have occurred and the resulting load-deformation graphs are all acceptable allowing for the linear nature of the solution schemes.

3.5 Conclusions

It appears from the analyses carried out on the individual steel and concrete elements and the test hinge, that the elements are working correctly and the hinge structure provides an adequate means of modelling the flexural behaviour of plastic hinge zones.

Chapter 4

PORTAL FRAME ANALYSES

4.1 Introduction

In this chapter the results obtained from static and dynamic simulations of ductile reinforced concrete portal frames, which form either reversing or uni-directional hinges, are analysed. Comparisons are made between results obtained from frames that are modelled solely by DRAIN-2DX beam-column elements and those which employ the hinge structure devised in Section 2.3 to represent the flexural behaviour of the plastic hinge zones. The effects of the formation of both hinge types and the resulting member elongations on the performance of the portal frames is also investigated.

4.2 The Portal Frame Structures

As the emphasis of this report is on structural analysis, a number of simplifying assumptions were made in the design of the portal frames. These assumptions, the design methods employed and the design forces and hinge element properties used can be found in Appendix A. Two frame types were subjected to both static and dynamic loads. One was designed to provide both gravity and seismic resistance and form uni-directional hinges, while the other was designed purely to sustain seismic loading and therefore form reversing hinges. In all analyses the cross-sectional dimensions of the structures were kept constant to ensure the resulting differences were only due to the loading variations (see Fig. 4.1). Each frame type was modelled in two ways; at first using only DRAIN-2DX beam-column elements, as in usual practice [11,12,13], and then employing the hinge structure devised in Section 2.3 to represent the plastic hinge zones within the frames. For the purpose of this chapter the first model type will be referred to as a 'beam-column' model and the second as a 'hinge' model.

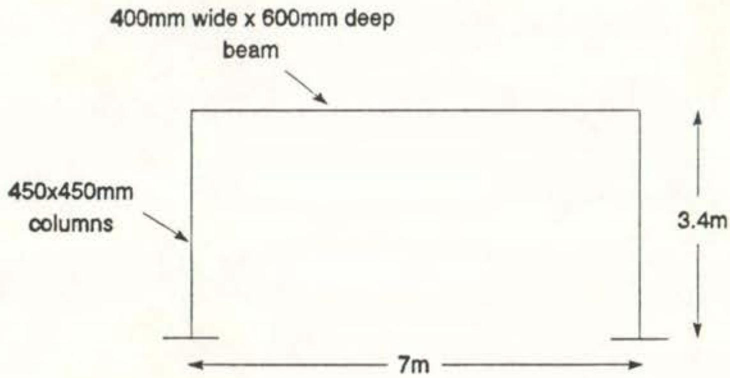

Fig. 4.1 Portal Frame Structure

4.3 Static Analyses

Equal lateral forces were applied at each end of the beam to introduce the equivalent seismic forces. These were incrementally increased until the lateral deflection of the mid point of the beam was six times the lateral deflection found in the modal analyses of the structure. The forces were then reversed twice, until first an equivalent negative and then an equivalent positive displacement was achieved. The flexural strength of the columns at the base of the structure was scaled as recommended in the commentary to NZS 3101 [9]. This increase in strength reduced the displacement ductility to approximately 3.5 and 4 for the uni-directional and reversing hinge models respectively.

The force-displacement relationships predicted by both the uni-directional hinge frame and the reversing hinge frame models are illustrated in Figs. 4.2 and 4.3. The graphed displacement value is the average of the displacements measured at either end of the frame. For both frame types the displacements predicted by the hinge models are almost identical to those predicted by the beam-column models. It is also apparent from the figures that the force required to push the uni-directional hinge frame to the 3.5 ductility displacement is greater than that required to push the reversing hinge frame to the same displacement value. This difference occurs because of the extra strength in the uni-

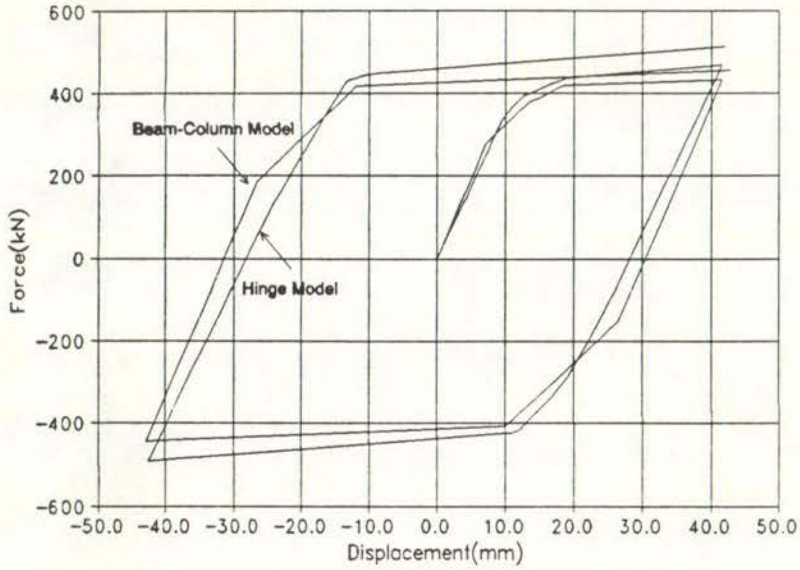

Fig. 4.2 Force versus Displacement Curves for Static Analysis of the Uni-directional Hinge Frames

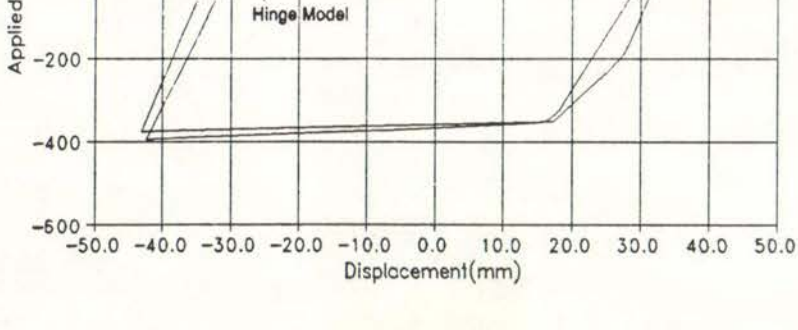

Fig. 4.3 Force versus Displacement Curves for Static Analysis of Reversing Hinge Frames

directional hinge frame, caused by the additional axial load in the beam, which results from the gravity loading.

The differences between the two model predictions became apparent when the beam elongations were calculated. The beam-column model does not predict any beam elongations for either frame type, while the hinge model showed a 30mm beam elongation for the uni-directional hinge frame and a 9.3mm beam elongation for the reversing hinge frame. These values are illustrated in Figs. 4.4 and 4.5. The elongation obtained from the reversing hinge frame is less than would be expected according to experimental results [1,2,3]. This anomaly is due to the fact that the hinge structure employed to model the plastic hinge zones does not allow for the shear resistance mechanism that develops in these regions, which experimental findings have shown makes a major contribution to the deformation in reversing hinges.

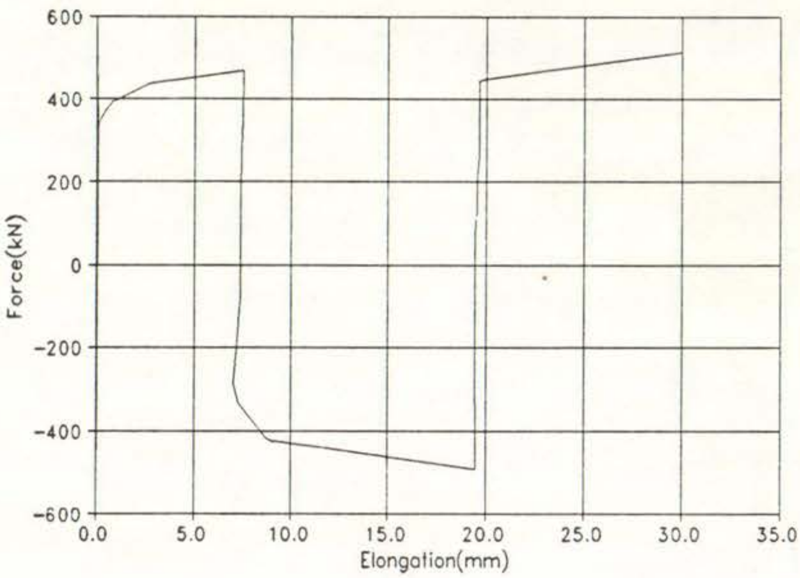

Fig. 4.4 Force versus Elongation Curves for Static Analysis of Uni-directional Hinge Frame

The type of hinge formed is reflected in the pattern of the force-elongation plots. After the formation of uni-directional hinges, any subsequent load reversals result in an accumulation of the inelastic rotations sustained by the hinge zones, as discussed in Section 2.1.2. This leads to a steady increase in the overall elongation of the member as evident in Fig. 4.4. In reversing hinges, a load reversal results in a reversal of the inelastic rotations sustained by the plastic hinge zones. Experimental results [1,2,3] have shown that the longitudinal reinforcement in the compression zone of the hinge does not

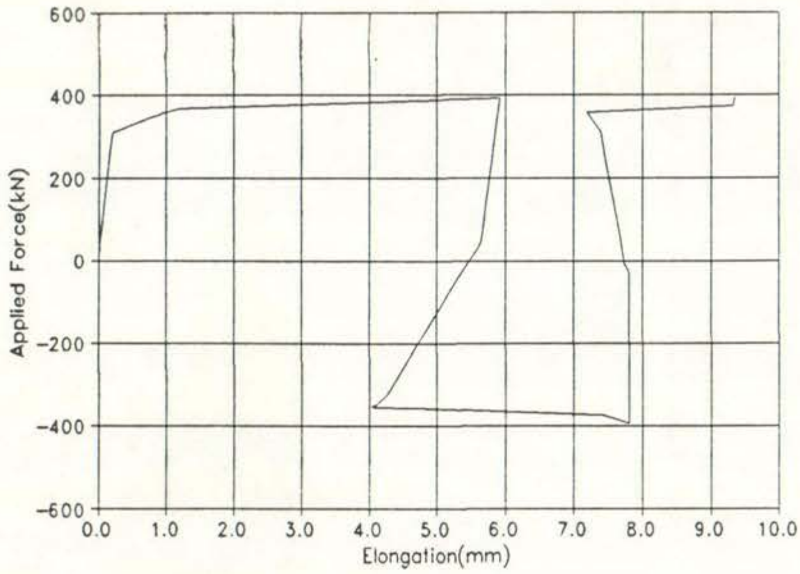

Fig. 4.5 Force versus Elongation Curves for Static Analysis of Reversing Hinge Frame

fully yield back during each load reversal and so under cyclic conditions there is an overall longitudinal elongation from one cycle to the next, as described in Section 2.1.3. Two factors responsible for this action are firstly a wedging type action of the concrete aggregate particles and secondly the shear resistance mechanism of the hinge zone. Although the hinge model employed makes some allowance for the aggregate wedging action, it does not model the shear resistance mechanism. As a consequence the compression zone reinforcement yields back to a greater degree than the experimental test results suggest. Thus the overall longitudinal elongation from one load reversal to the next does not occur to the same extent. This behaviour is evidenced in Fig. 4.5.

Table 4.1 compares the elongations obtained from the DRAIN-2DX analysis and those predicted using equations 2.2 and 2.3, as derived by Fenwick and Megget [1,2,3] from experimental results for both frames types.

The variable 'e' represents the elongation of the longitudinal reinforcement in the compression zone. As can be seen from the table the results obtained from the DRAIN-2DX analysis compare favourably with those obtained from the empirical equations.

Table 4.1 Comparison of Predicted Beam Elongations

	Equation Prediction	Hinge Model Prediction
Uni-directional Hinge	29.89 mm	30.0 mm
Reversing Hinge	5.91 + e mm	9.3 + e mm

Comparing the maximum column reactions that developed during the static analyses of the hinge models with those that developed in the beam-column models, increases in bending moments, shear forces and axial forces of up to 15% were observed.

It is important to note that the Draft Loadings Code [10] allows for displacements of up to two and a half percent of the inter-storey height. Consequently the portal frame can deflect up to 85mm and still be within the bounds of acceptability. The displacements obtained from these static analyses are therefore only 47% of the maximum allowable displacements. Hence, it is highly probable that the beam elongations resulting from analyses involving greater frame displacements would be in excess of those obtained here, as would be the forces induced within the columns.

4.4 Dynamic Analyses

The first 20 seconds of the El Centro 1940, North-South earthquake ground motion record was employed for the dynamic analyses of the portal frames. A time step of 0.004 seconds was used in all the analyses. The horizontal displacement-time histories, recorded at both ends of the beam, for both the uni-directional and reversing hinge model frames, are illustrated in Figs. 4.6 and 4.7 respectively. The resulting beam elongation is also displayed on both figures.

The total member elongation at the end of the dynamic loading sequence was approximately 22.4mm for the uni-directional hinge frame and 8.4mm for the reversing

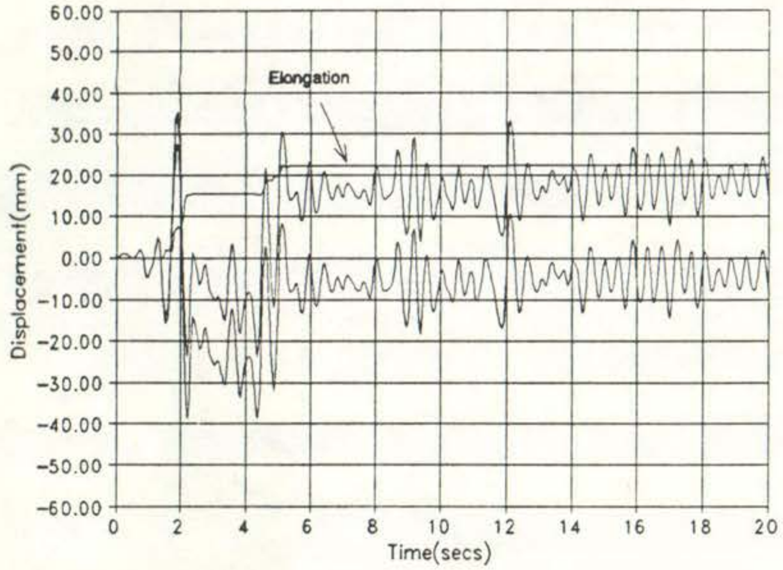

Fig. 4.6 Hinge Model Displacement-Time History for the Unidirectional Hinge Frame

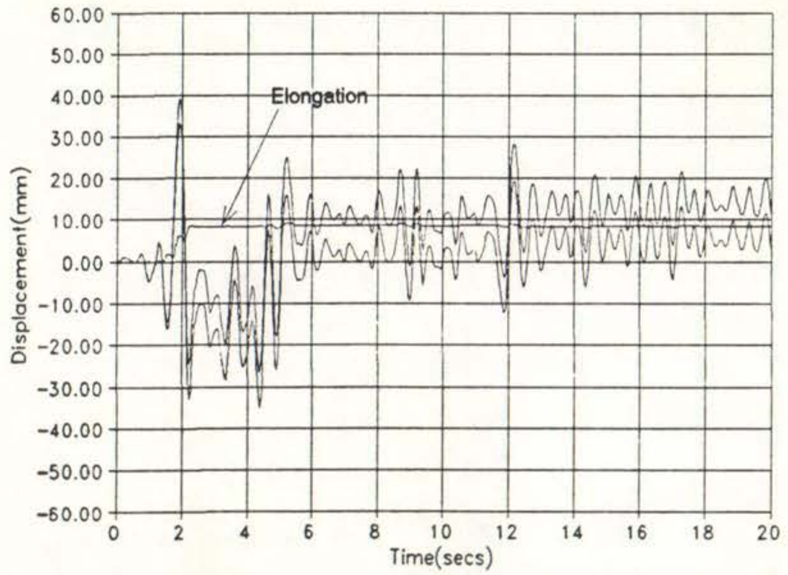

Fig. 4.7 Hinge Model Displacement-Time History for the Reversing Hinge Frame

hinge frame. The magnitude of the elongation of the beam in the uni-directional hinge frame falls in the same region as experimental results suggest [1,2,3], however the magnitude of the elongation of the beam in the reversing hinge frame is significantly less than would be expected. This anomaly again arises because the hinge structure employed to represent the behaviour of the plastic hinge zones is only designed to model flexural behaviour and can not represent the shear effects induced within the reversing hinge zones, as discussed in Section 4.2.

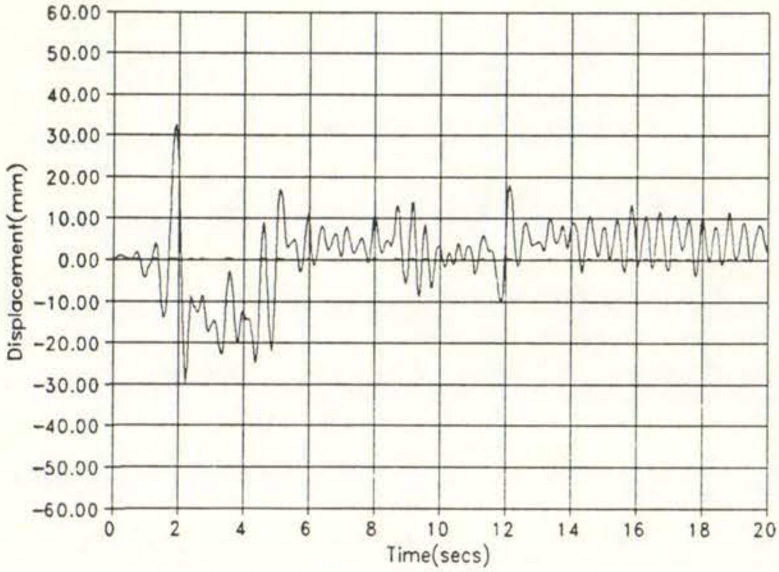

Fig. 4.8 Beam-Column Model Displacement-Time History for the Uni-directional Hinge Frame

For the purpose of comparison, the displacement-time histories resulting from tests on the beam-column frame models are shown in Figs. 4.8 and 4.9. As is evident from both figures the beam-column element model predicts no overall beam elongation.

Once again, the maximum reactions induced in the columns during the seismic loading of the portal frames were greater for the hinge models than for the beam-column models. The most dramatic increase observed was the axial force in the reversing hinge model frame which exceeded that in the beam-column model by 29%.

As in the static analyses, the maximum displacements obtained are less than half that allowed by the Draft Loadings Code [10] and the ductilities achieved are approximately 3.5 and 4 for the uni-directional and reversing hinge frames respectively. Thus greater beam elongations and column forces could be expected if the frames were subjected to

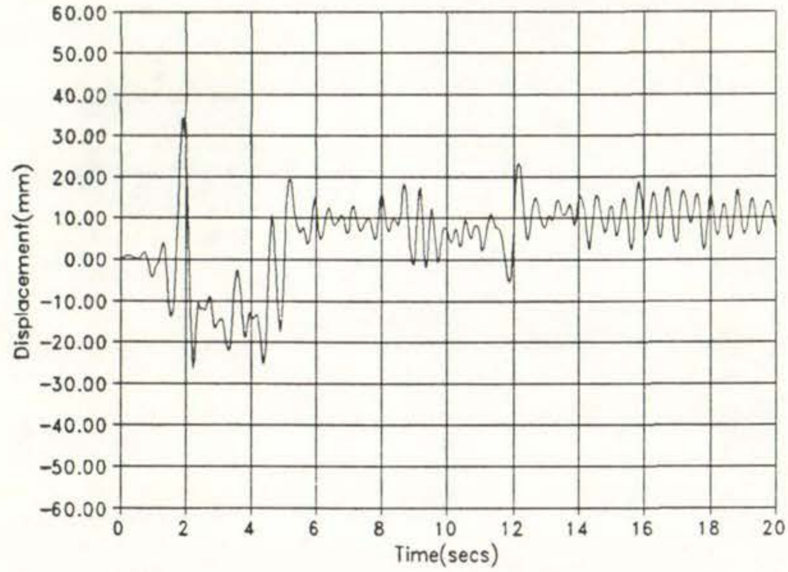

Fig. 4.9 Beam-Column Model Displacement-Time History for the Reversing Hinge Frame

forces which caused displacements closer to those allowed by the code.

Chapter 5

MULTI-STOREY FRAME ANALYSES

5.1 Introduction

This chapter analyses the results obtained from static and dynamic simulations of ductile reinforced concrete two bay two storey frames. As in chapter four, two models are used to predict the behaviour of the frame structures; one that is composed completely of DRAIN-2DX beam-column elements and one that employs the hinge structure devised in Section 2.3 to represent the flexural behaviour of the plastic hinge zones. Comparisons are then drawn between the two sets of results. The effects of the formation of both reversing and uni-directional plastic hinges and the associated member elongations on the performance of the frame structures is also investigated.

5.2 The Multi-Storey Frame Structures

As in the portal frame analysis, two types of frame structures were subjected to both static and dynamic loads. One was designed to sustain gravity loads, provide seismic resistance and form uni-directional hinges, and the other was designed to sustain only seismic actions and thus form reversing plastic hinges. Once again the cross-sectional dimensions of the structures were kept constant to ensure that the resulting differences were only due to the loading variations (see Fig. 5.1).

Each frame type was again modelled in two ways; initially using only DRAIN-2DX beam-column elements, and then employing the hinge structure devised in Section 2.3 to represent the plastic hinge zones within the frames. For the purpose of this chapter, the first model will again be referred to as a 'beam-column' model and the second as a 'hinge' model.

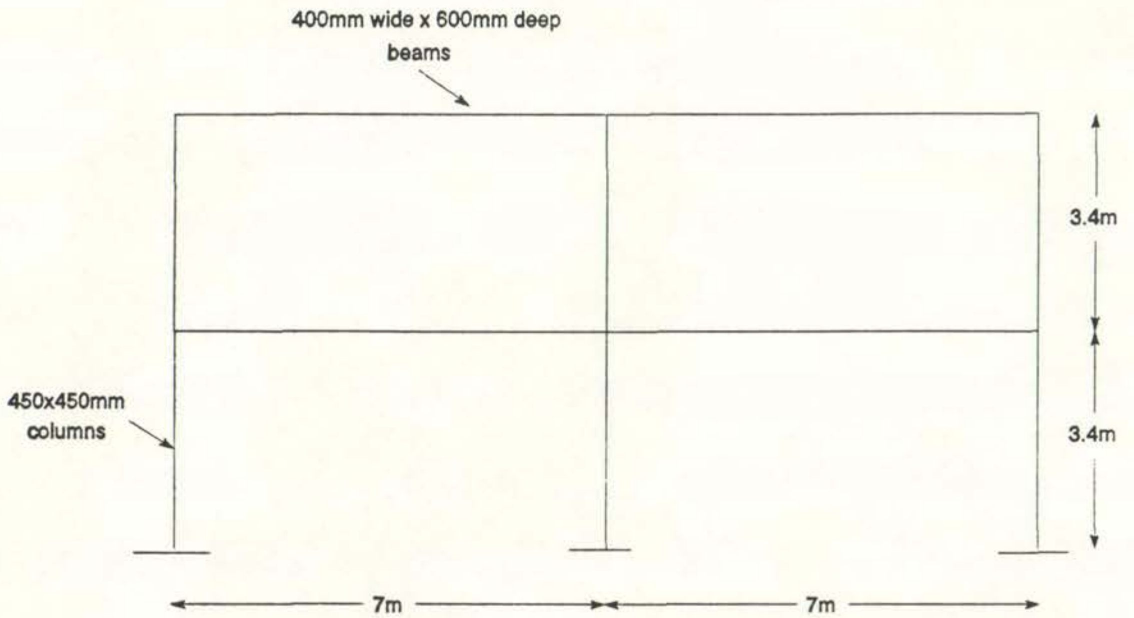

Fig. 5.1 Multi-Storey Frame Structure

DRAIN-2DX was used to perform a response spectrum analysis on the basic frame structure. Firstly the mode shapes and frequencies were obtained from an eigenvalue analysis. Then the Draft Code response spectrum, corresponding to a structural ductility factor of one, was scaled to an equivalent ductility six spectrum and utilised in the response spectrum analysis. The gravity analysis of the frame was carried out using the computer package PFRAME. As with the portal frame analysis, a number of simplifying assumptions were made in the design of the frame structures. Appendix B sets out these assumptions, the design methods employed and the design forces and hinge element property calculations for both frame types.

5.3 Static Analyses

DRAIN-2DX was used to perform step-by-step equivalent static earthquake analyses. The seismic forces were calculated according to the Draft Loadings Code [10]. The uni-directional hinge frame was initially gravity loaded. Both frames were then incrementally loaded until the lateral deflection at the intersection point of the level two beams was six times the lateral deflection obtained at that location from the modal analysis. The load was applied to the internal and external columns in a ratio of two to one respectively. The flexural strength of the columns was then scaled as recommended in the commentary to NZS 3101 [9]. This increase in strength reduced the displacement ductility to approximately four for the hinge model frames and five for the beam-column model frames.

The resulting force-displacement graphs for both the uni-directional and the reversing hinge frames are illustrated in Figs. 5.2 and 5.3 respectively. The graphed displacement is the average of the displacements at either end of the frame level.

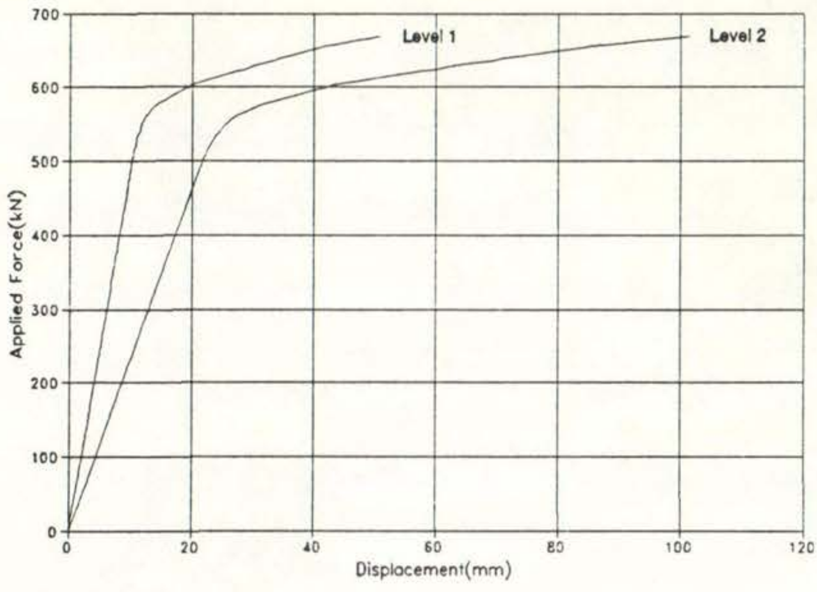

Fig. 5.2a Uni-directional Hinge Frame Force versus Displacement: Hinge Model

Comparing the graphs it is evident that, although the beam-column model predicts more angular force-displacement rate changes, the general shape of the curves for both frame types is very similar. The angularity of the beam-column model graphs can be accounted for by the fact that the force-displacement relationship associated with the DRAIN-2DX

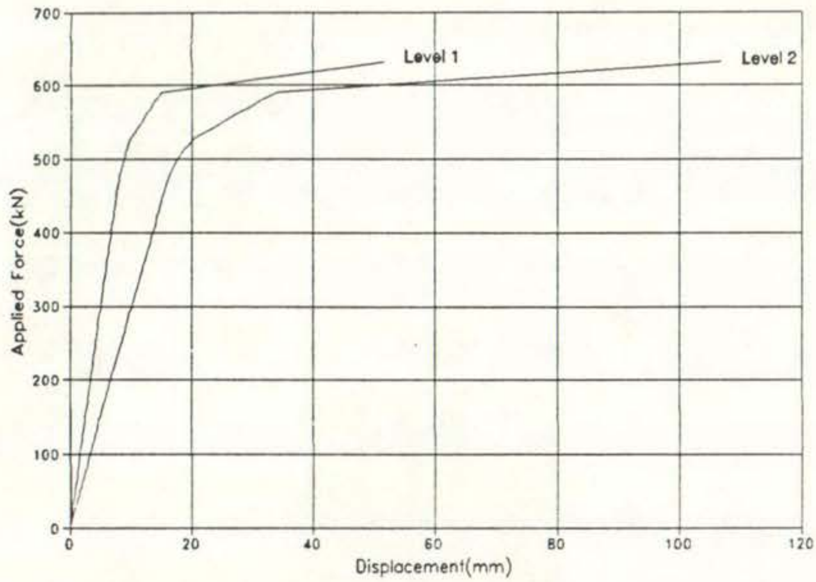

Fig 5.2b Uni-directional Hinge Frame Force versus Displacement: Beam-Column Model

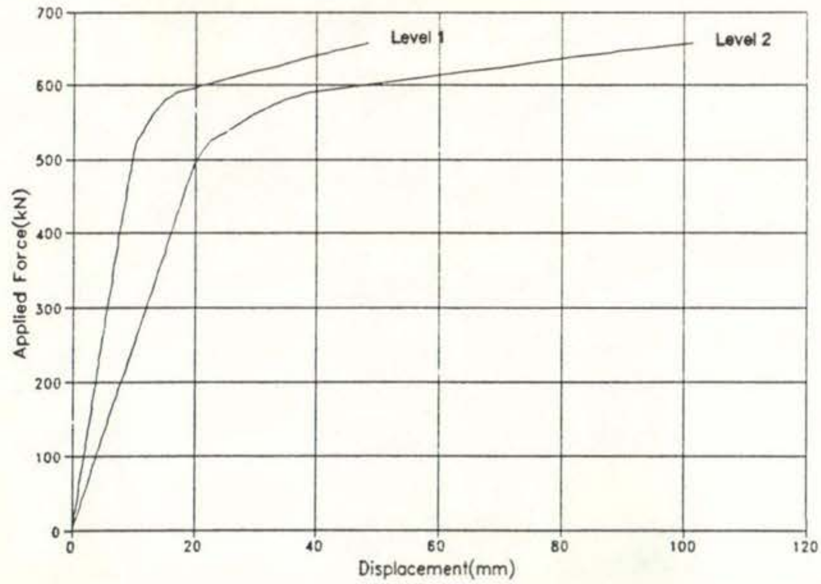

Fig. 5.3a Reversing Hinge Frame Force versus Displacement: Hinge Model

beam-column elements is very simple and contains only two possible stiffness variations, whereas the steel element force-displacement relationship, although piecewise-linear, approximates a curvilinear relationship and consequently produces a smoother force-

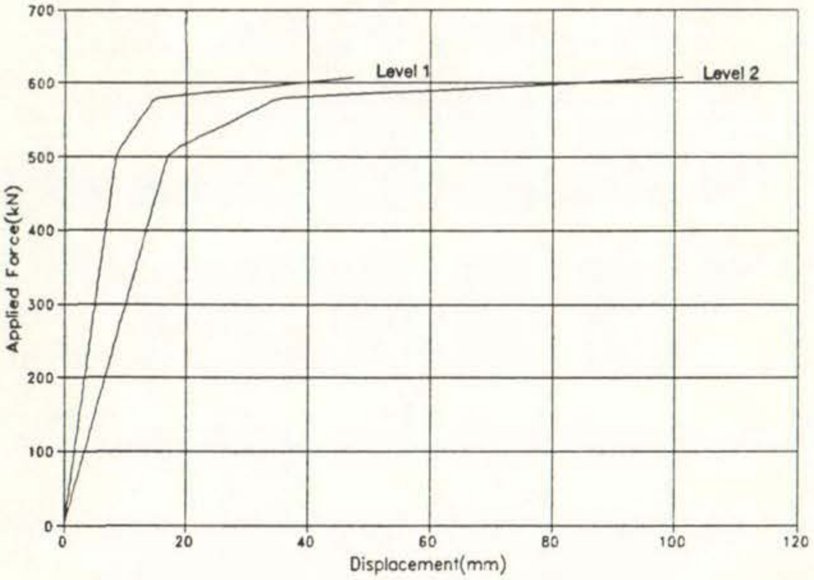

Fig. 5.3b Reversing Hinge Frame Force versus Displacement: Beam-Column Model

displacement graph. This difference could also account for the slightly larger forces required for the hinge model to reach a ductility of four, as opposed to those required for the beam-column model to achieve a ductility five displacement. In all four graphs the maximum level two displacement exceeds that of level one by more than 100%, which is as expected considering the applied load pattern.

Figs. 5.4 and 5.5 show the force-elongation graphs obtained from the uni-directional and reversing hinge frames respectively. The beam-column model does not predict any beam elongations, so only the hinge model predictions are illustrated.

The graph predicted by the uni-directional hinge frame appears smoother than that predicted by the reversing hinge frame. This is because there are twice as many hinge zones within the uni-directional hinge frame and consequently the yielding that occurs is dispersed over a greater number of elements resulting in a more gradual change from elastic to plastic displacements. The maximum elongation obtained for level one exceeds that obtained for level two by approximately 200% for the uni-directional hinge frame and 40% for the reversing hinge frame. In the uni-directional hinge frame, this

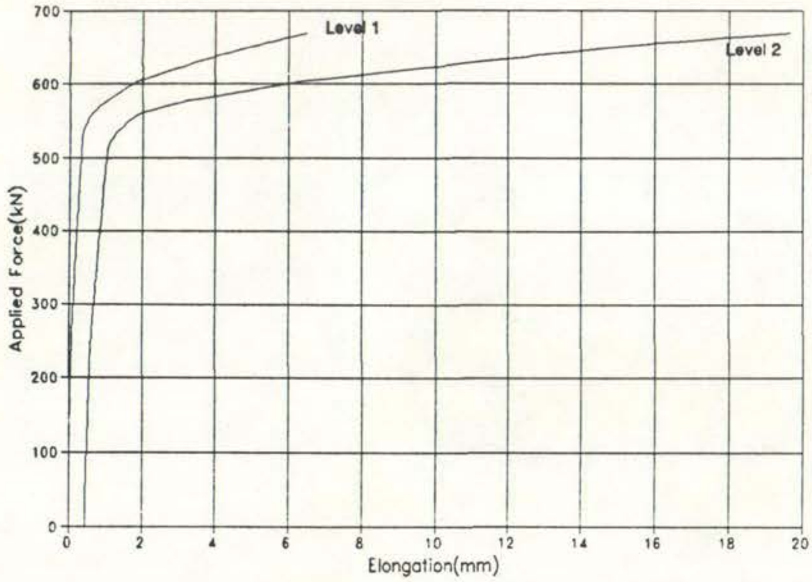

Fig. 5.4 Uni-directional Hinge Frame Force versus Elongation: Hinge Model

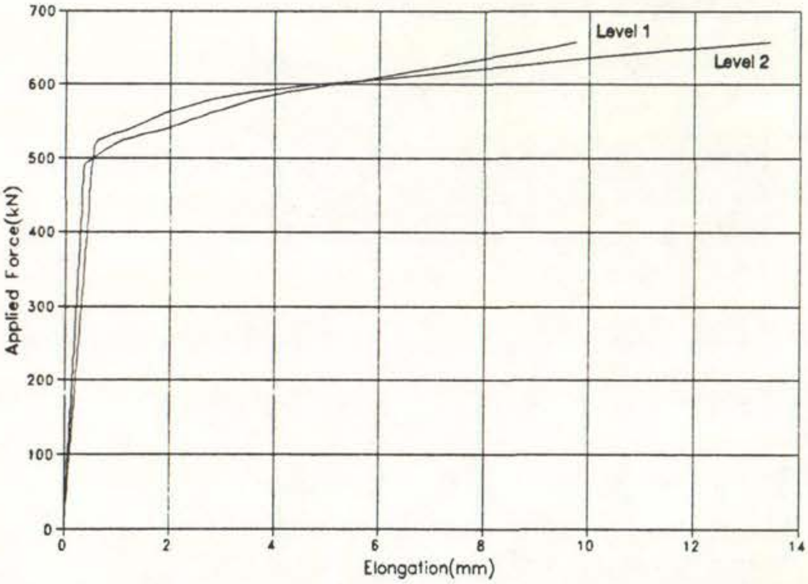

Fig. 5.5 Reversing Hinge Frame Force versus Elongation: Hinge Model

difference is partially due to the portal type action produced in level two as a result of the gravity loading. While in the reversing hinge frame, the rotations occurring within the level one plastic hinge zones are up to 120% in excess of those experienced by the level two hinges, thus accounting for the greater elongation value.

Table 5.1 compares the elongations obtained from the static simulations of the hinge models with those predicted using equations 2.2 and 2.3, where 'e' is the elongation of the longitudinal reinforcement in the compression zones of the plastic hinges. The table clearly shows that the elongations predicted by the hinge model compare very favourably with those obtained using the experimentally derived equations.

Table 5.1 Comparison of Predicted Beam Elongations

	Equation Prediction	Hinge Model Prediction
Uni-directional Hinge	Level One: 19.7 mm Level Two: 6.5 mm	Level One: 20.3 mm Level Two: 6.7 mm
Reversing Hinge	Level One: 13.5 + e mm Level Two: 9.8 + e mm	Level One: 13.9 + e mm Level Two: 9.7 + e mm

After analysing the maximum forces that developed in the columns during the static loading test, it is clear that the strength demands placed on the columns in the hinge model greatly exceed those of the beam-column model. In fact, the level one columns experienced bending moments of 70% and shear forces of 21% in excess of those experienced by the beam-column model. Once again, it is important to note that the inter-storey deflections are only about 60% of those allowed by the Draft Loadings Code [10]. It is highly probable therefore, that both greater elongations and column forces would develop if the multi-storey structures were displaced to values closer to the limiting inter-storey deflection imposed by the Code.

5.4 Dynamic Analyses

The frame structures, as described in Section 5.2, were subjected to the first 20 seconds of the **El Centro, 1940, North-South** earthquake ground motion record. A time step of 0.004 seconds was used in all the analyses. The resulting displacement-time histories for both the uni-directional hinge frames and the reversing hinge frames are illustrated in Figs. 5.6 and 5.7 respectively.

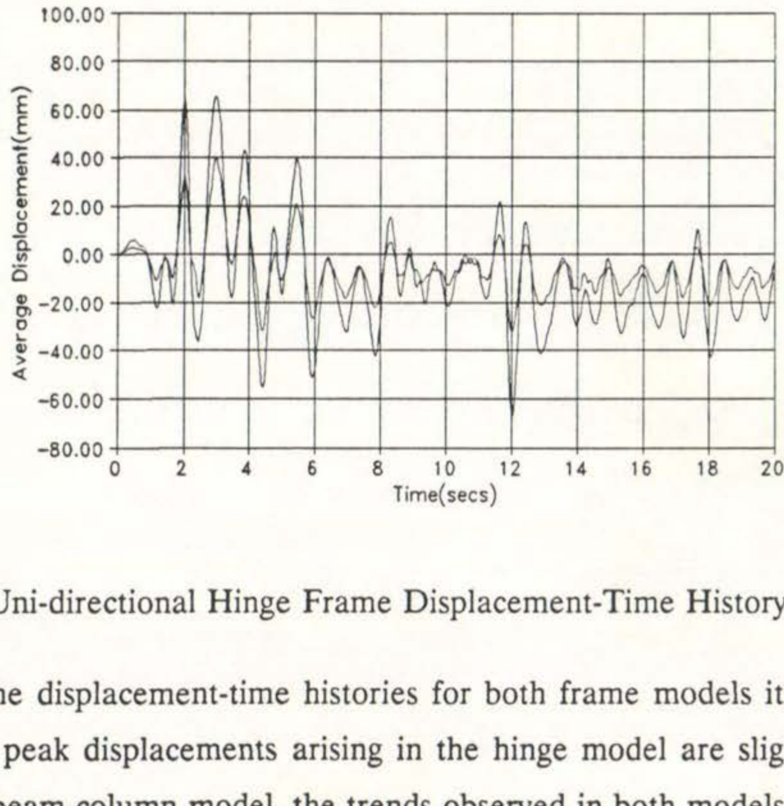

Fig. 5.6a Uni-directional Hinge Frame Displacement-Time History: Hinge Model

Comparing the displacement-time histories for both frame models it is apparent that although the peak displacements arising in the hinge model are slightly greater than those in the beam-column model, the trends observed in both models are very similar. The displacements resulting from the uni-directional hinge frame are generally slightly less than those resulting from the reversing hinge frame because of its greater strength. This is due to the increased axial loads in the beams resulting from the gravity loading. The level one displacements are less than those obtained for level two as would be expected.

The elongation-time histories for the uni-directional and reversing hinge frames are

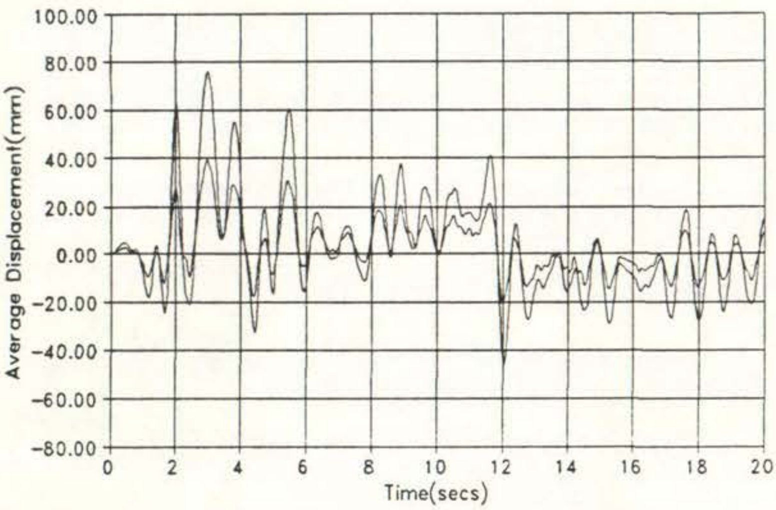

Fig. 5.6b Uni-directional Hinge Frame Displacement-Time History: Beam-Column Model

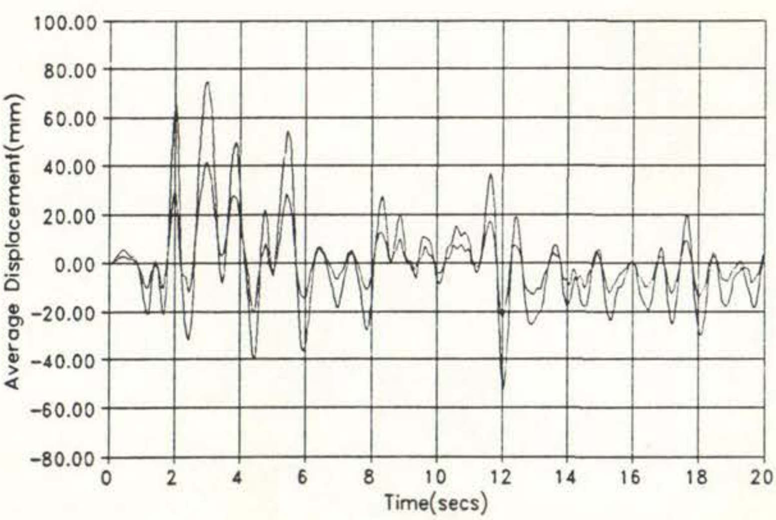

Fig. 5.7a Reversing Hinge Frame Displacement-Time History: Hinge Model

illustrated in Figs. 5.8 and 5.9 respectively. As can be seen from the graphs the level one elongations exceed those arising in level two by approximately 130% for the uni-directional hinge frame and 65% for the reversing hinge frame. These differences occur

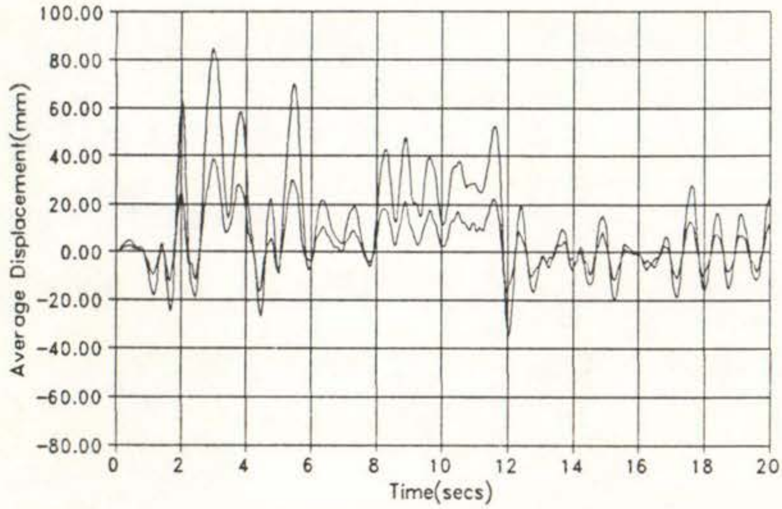

Fig. 5.7b Reversing Hinge Frame Displacement-Time History: Beam-Column Model

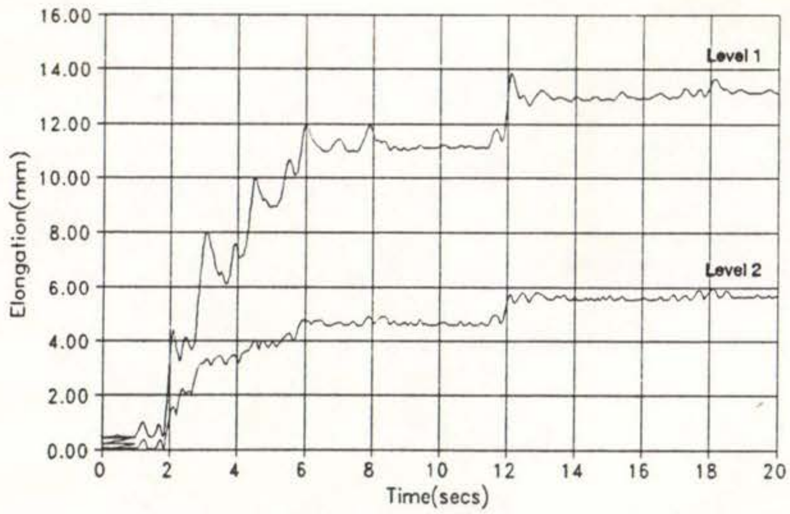

Fig. 5.8 Uni-directional Hinge Frame Force-Elongation Graph: Hinge Model

as a result of the portal type action arising in the uni-directional hinge frame and the greater rotations experienced in the level one plastic hinge zones of the reversing hinge frame, as discussed in Section 5.3. There also appears to be a significant amount of

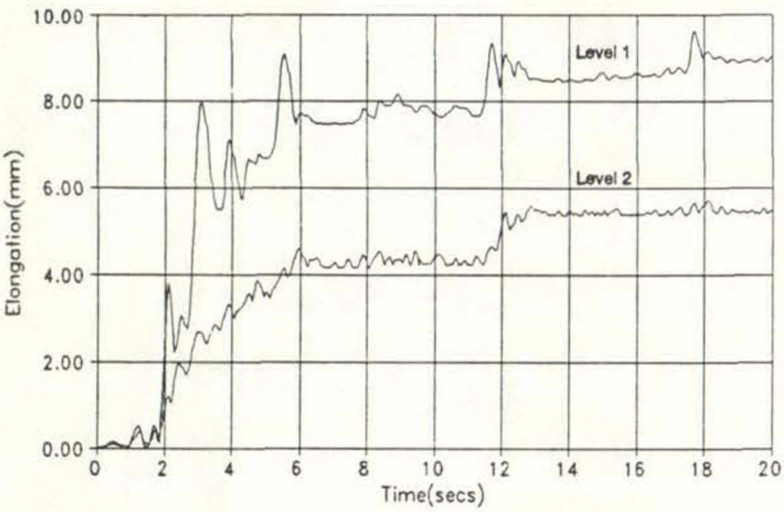

Fig. 5.9 Reversing Hinge Frame Force-Elongation Graph: Hinge Model

'elongation-contraction' vibrations occurring in both frames. These vibrations can be accounted for by the elastic unloading-reloading cycles occurring within the hinge steel element (refer to Fig. 3.2). The general trend of both graphs is for the elongation to increase with time, although the rate at which it increases declines dramatically over the length of the earthquake record. Comparing this trend with the El Centro ground acceleration record it is clear that the rapid elongation increase over the first five seconds of the elongation-time history corresponds to the greater ground accelerations experienced during the equivalent period of the earthquake record. The maximum elongation of the uni-directional and reversing hinge frames for the twenty second period occurred at level one and was 13.15mm and 9.05mm respectively. Once again the elongation of the reversing hinge frame is less than would be expected, because the hinge structure employed to model the plastic hinge zone only models flexural behaviour, as discussed in Section 4.3.

As in the static analyses, comparisons of the maximum forces induced in the columns during the dynamic loading sequences were made. These indicated that forces in the hinge model were about 5% in excess of those that developed in the beam-column model. Although this is not a large increase, it must be noted that not only were the maximum inter-storey deflections about 47% of those allowed by the Draft Loadings Code [10], but that the ductility demands placed on the structures were only about 45% of the ductility six displacements that they were designed for. These small values again lead to the supposition that had the frames reached displacements closer to or in excess of the values that they had been designed for, then the resulting beam elongations and column forces would have been far greater than those obtained in this study.

Chapter 6

SUMMARY AND CONCLUSIONS

6.1 Portal Frame Analyses

The portal frame analyses for the uni-directional hinge frame gave elongations of 30mm and 22.4mm for the static and dynamic analyses respectively. For the reversing hinge frame an elongation of 9.3mm was obtained from the static analysis and 8.4mm occurred in the dynamic analysis. The elongations resulting from both the static analyses agreed well with those calculated from the empirical equations for predicting beam elongations [1,2,3] where the effects of shear are neglected. The elongations resulting from the reversing hinge simulations are considerably smaller than experimental results [1,2,3] suggest occur because only the flexural behaviour of the plastic hinge zones has been modelled.

The deflections obtained from the analyses of the portal frame were less than half that allowed by the Draft Loadings Code, so the possibility exists that larger beam elongations would have developed if the structures were deflected to values closer to that allowed by the code. In all the analyses, it was clearly evident that the resulting beam elongations increased the magnitude of the bending moments and shear forces induced in the columns.

6.2 Multi-Storey Frame Analyses

For both the uni-directional and the reversing hinge frames, the maximum beam elongations occurred on level one. For the static analyses these values were 19.7mm and 13.5mm for the uni-directional and reversing hinge frames respectively, and for the dynamic analyses they were 13.2mm and 9.1mm respectively. These elongations are considerably less than expected, even allowing for the fact that only the flexural behaviour of the plastic hinge zones was modelled. Results obtained by Davidson and Fenwick [14], suggest that much larger beam elongations (than those obtained in this study) could occur. However, when reviewing the elongations obtained for the multi-storey structures in this report, it is important to note that in the static analyses the structures only reached a ductility four displacement and in the dynamic analyses they only reached displacements corresponding to a ductility of approximately 2.6. Coupled with this, the inter-storey deflections obtained in both analyses were up to 53% less than the allowable Draft Loadings Code values [10]. Finally, it must also be noted that, even considering the low beam elongation values obtained in this study, the bending moments and shear forces sustained by the columns still increased.

6.3 The Hinge Model

(i) A computer model of a plastic hinge zone in a reinforced concrete beam has been developed and incorporated into a dynamic analysis program. It provides a practical means of predicting elongation effects, which arise due to flexure, in the dynamic analysis of frame structures.

(ii) The model allows for the change in steel properties of the reinforcement associated with yielding and the Bauschinger effect. It also allows for limited crushing of the concrete and the 'wedging action', which arises in beams due to dislocated aggregate particles which become wedged in the cracks. The properties of the concrete and steel elements making up the hinge model have been based on cyclic tests of concrete, reinforcement and reinforced concrete prisms, carried out at Auckland in a previous research project.

(iii) The model allows for the effect small axial loads have on the flexural resistance and the elongation that occurs due to flexure.

(iv) The model does not allow for the effects of shear on the behaviour of plastic hinge zones. Experimental work [1,2,3] shows that shear has a major influence on both the load deflection characteristics and the elongation that develops in reversing plastic hinge zones. Typically this experimental work has indicated that the elongation associated with flexure is of the order of one third that of the resultant elongation. To enable realistic elongations to be predicted in reversing hinge zones the effect of shear must be included in the model.

6.4 Further Work Requirements

(i) Develop the plastic hinge structure so that it models both shear and flexural behaviour.

(ii) Use the improved plastic hinge structure to perform further analyses to assess more accurately the magnitude of beam elongations and the effects of these elongations on the response of the structures.

(iii) Analyse a greater range of structures.

(iv) Examine the factors contributing to beam elongations in more detail and develop a design method which makes allowances for this phenomenon.

References

1. FENWICK, R.C., "Member Elongation - A Neglected Factor in Seismic Design", N.Z. Concrete Society Technical Report TR10, 1990, pp 89-94.

2. FENWICK, R.C., "The Behaviour of Plastic Hinge Zones in Seismic Resistant Concrete Structures", Earthquake Blast and Impact S.E.C.E.D. Conference Proceedings, 1991, Elsevier Applied Science, London, pp 221-230.

3. FENWICK, R.C. and MEGGET, L.M., "Elongation and Load Deflection Characteristics of Reinforced Concrete Members Containing Plastic Hinges", Bulletin of N.Z.N.S.E.E., proposed Vol.26 No.1, March 1991.

4. ALLAHABADI, R., "DRAIN-2DX - Seismic Response and Damage Assessment for 2D Structures", Doctor of Philosophy Thesis, University of California, Berkeley, 1987.

5. TJOKRODIMULJO, K., "Behaviour of Reinforced Concrete Under Cyclic Loading", University of Auckland, School of Engineering Report No. 374, February 1985.

6. MENEGOTTO, M. and PINTO, P.E., "Method of Analysis for Critically Loaded Reinforced Concrete Plane Frames Including Changes in Geometry and Non-Elastic Behaviour of Elements under Combined Normal Force and Bending", IABSE, Symposium on the Resistance and Ultimate Deformability of Structures Acted on by Well-Defined Repeated Loads, Lisbon, 1973.

7. BOLONG, Z., MINGSHUN, W. and KUNLIAN, Z., "A Study of Hysteretic Curves of Reinforced Concrete Members under Cyclic Loading", Proc. of the 7th World Conference on Earthquake Engineering, Istanbul, Turkey, September 1980.

8. ALLAHABADI, R. and POWELL, G.H., "DRAIN-2DX User Guide", Earthquake Engineering Research Centre, University of California, Berkeley, Report No. EERC 88-06, 1988.

9. Standards Association of New Zealand, "Code of Practice for the Design of Concrete Structures", NZS3101: Parts 1 and 2, 1982.

10. Standards Association of New Zealand, "Draft Code for General Structural Design and Design Loadings for Buildings", DZ 4203/4, March 1989.

11. DAVIDSON, B.J., FENWICK, R.C. and CHUNG, B.T,, "P-Delta Effects in Multi-Storey Structural Design", 10.W.C.E.E. Madrid, July, 1992

12. FENWICK, R.C. and DAVIDSON, B.J., "Dynamic Behaviour of Multi-Storey Buildings", The University of Auckland Research Report No.463, Department of Civil Engineering, University of Auckland, 1991

13. FENWICK, R.C. and DAVIDSON, B.J., "Comparative Analyses of Multi-Storey Frames and Walls Using the Current Draft Loadings Code", Bulletin of N.Z.N.S.E.E, Vol 22, No. 4, 1989

14. FENWICK, R.C. and DAVIDSON, B.J., "The Seismic Response of a Ductile Reinforced Concrete Frame with Non-Reversing Hinges", The University of Auckland Research Report No.527, Department of Civil Engineering, University of Auckland, 1993 Jan.

Appendix A

PORTAL FRAME DESIGN

A.1 Assumptions

1. The portal frame was sized to satisfy seismic related stiffness requirements in the draft code.
2. Torsional effects were not considered so the analyses could be carried out on a two dimensional frame.
3. Initial yield strengths used in the analyses were calculated using the Draft Loadings Code. The yield strengths which could form in a real structure due to the application of minimum steel quantities required by the steel code were not taken into account.
4. The concrete strength was assumed to be 30 MPa at 28 days and to have an average strength within the structure of 39 MPa. The elastic modulus was taken to be 29350 MPa and the shear modulus as 11740 MPa.
5. The portal frame was assumed to be one employed in a 3-bay, 6 storey building which has a seismic mass per floor of 5100 kN [14].
6. P-delta effects were not considered.

A.2 Design

A.2.1 Member Properties

Column Properties

Size: 450 mm x 450 mm

A = cross-sectional area = Ag = 450 x 450 = 202500 mm^2

SA = shear area = 5/6 Ag = 168750 mm^2

E = youngs modulus = $4700\sqrt{39} \approx 29350$ MPa

Shear Modulus = 0.4E = 11740 MPa

Beam Properties

Size: 400 mm wide x 600 mm deep

Composite action assumed:

I = second moment of area = Ig/2 = 4627.3×10^6 mm^4

A = cross-sectional area = Ag/2 = 136875 mm^2

SA = shear area = 5/6 A = 114062.5 mm^2

d = distance between centroids of beam reinforcement = 540 mm

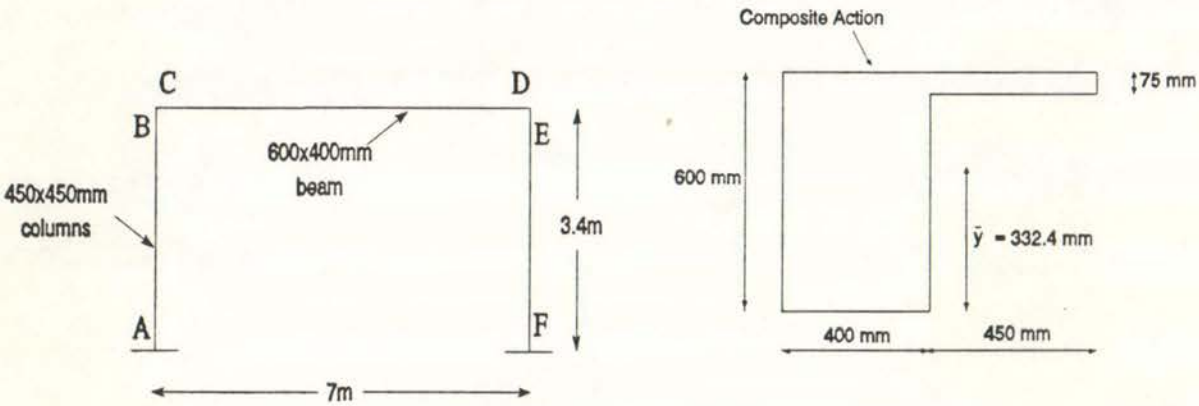

Fig. A.1 Portal Frame Structure

A.2.2 Loading

Gravity Loads per Floor

Dead Load:

columns = 20 x 24 x 3.4 x 0.45^2 = 331 kN

beams = 15 x (7-0.45) x 0.6 x 0.4 x 24 = 652 kN

16 x (7-0.45) x 0.6 x 0.4 x 24 = 604 kN

floor = (0.4+0.2+0.2) x (28x21) = 470 kN

cladding = 1.2 x 3.4 x (21+28) x 2 = 400 kN

200 dycore + 65mm topping

$$= (2.4 + 24 \times 0.065) \times 3 \times (28-0.4) \times (7-0.4) = 2164\text{kN}$$

Total Dead Load = 4621 kN

Live Load:

Seismic Live Load = 5100 - 4621 = 479 kN = 0.815 kPa

From 2/DZ 4203 $\omega_t = D + \psi L$, where $\psi = 0.4$

$$\text{Total Live Load} = \frac{0.815}{0.4} = 2\text{kPa}$$

Gravity Load per Bay

Dead Load:

beams = 0.6 x 0.4 x 24 = 5.8

floor = 4 x (7 - 0.4) = 26.4

sundry = 0.8 x 7 = 5.6

Total Dead load/Bay = 37.8 kN/m

From 2/DZ 4203 $R = 0.4 + \dfrac{2.7}{\sqrt{7 \times 21}} = 0.623$

$$\text{Total Gravity Load per Bay} = \omega_D + \psi RL = 37.8 + (7 \times 2 \times 0.623 \times 0.4)$$

$$= 41.3 \text{ kN/m}$$

Transitional mass per frame

$$\text{Translational mass per frame} = \frac{1}{3} \times \frac{5100}{9.81} = 173.3 \ \frac{\text{kNs}^2}{\text{m}}$$

A.2.3 Seismic Force

Stiffness of the structure:

$$k = \frac{P}{\Delta} = \frac{2 \times 173.3 \times 1.5 \times 0.4}{\left(3.568 \times 10^{2} + 3.9209 \times 10^{-2}\right) / 2} = 51653.209 \ \frac{kN}{gm}$$

The values for P and Δ were obtained from a static push over test carried out using DRAIN-2DX

Period of the structure:

$$T = 2\pi \sqrt{\frac{m}{k}}$$

$$= 2\pi \sqrt{\frac{173.3}{51653.209}} = 0.364 \text{ sec}$$

Mass proportional damping ratio:

$$A = 2 \xi \omega$$

$$= 2 \times 0.05 \times \frac{2\pi}{T} = 1.7266$$

From the Draft Loadings Code [10] for a normal soil in the Wellington region and a structure ductility of six.

$$C_o = 0.2144$$

$$C_d = C_o R Z$$

$$= 0.2144 \times 1.0 \times 0.8 = 0.17152$$

Thus the horizontal seismic force is:

$$V = C_d \times W_t$$

$$= 0.17152 \times 1700 = 291.6 \text{ kN}$$

A.2.4 Strain Hardening Properties

After analysing data gathered from numerous tests on ductile structures the following rules were developed in order to determine the proportion of strain hardening occurring within a plastic hinge zone.

1. For hinges that form in regions with large moment gradients the post yield moment increment is 3.75 times the yield moment, per radian of rotation.
2. For hinges that form in regions with small moment gradients the post yield moment increment is equal to the yield moment, per radian of rotation.

As a result the following formulas were employed to calculate the strain hardening ratios of the elements within the frames.

For the columns: $\alpha = \dfrac{\beta\, M_i\, L_{eff}}{3\,E\,I}$

For the beam-column yielding elements: $\alpha = \dfrac{\beta\, M_i\, L_{eff}}{3\,E\,I}$

For the steel elements within the hinge structure: $\alpha = \dfrac{\beta\, M_i\, L_{eff}}{d^2\, E_s\, A_s}$

where:

d = distance between the centroids of the top and bottom reinforcement

E = Concrete Modulus

I = Second moment of area

E_s = Steel Modulus

A_s = Cross-sectional area of the steel element

L_{eff} = L , for all the columns

= L' , for the beams

$L' = \frac{L}{2}$, for all unloaded beam-column elements

$= \sqrt{\frac{2 M_{span}}{\omega}}$, for loaded span hinge beam-column elements

$= x - \sqrt{\frac{2 M_{span}}{\omega}}$, for loaded column face hinge beam-column elements

= L x length scale factor for all the steel hinge elements

ω = gravity load/m

x = distance between $M_{column\,face}$ and M_{span}

M_i = the design moment

β = 3.75 or 1.0 depending on the region the hinge forms in, as described previously

A.2.5 Hinge Structure Property Rules

The following rules were developed in order that the hinge model as a whole have the same stiffness as the remainder of the frame structure.

For the steel and concrete elements:

1. $A_c \geq A_{section}/2$
2. $M_i = A_s f_y d$
3. $A_s d^2 n \geq I$ section

where:

A_c = cross-sectional area of the concrete element

f_y = yield stress of the steel

n = E_s/E_c

For the shear connection element:

$$\frac{EA}{L} \text{ shear connection} < \frac{EA}{L} \text{ beam}$$

$$EI \text{ shear connection} \approx EI \text{ beam x } 10^{-3}$$

$$\frac{EI}{L} \text{ shear connection} \approx 0.35 \frac{EI}{L} \text{ beam}$$

$$\frac{EI}{L^3} \text{ shear connection} \approx 875 \frac{EI}{L^3} \text{ beam}$$

A.2.6 Design Moments

The seismic and gravity design moments were calculated using moment distribution. The gravity load was taken as 41.3kN/m (see Section A.2.2). The centre-line values obtained are illustrated in Table A.1. Points A to F refer to the positions on the frame where the moments occur (see Fig. A.1).

Table A.1 Design Moments

Moments-kNm	A	B	C	D	E	F
Seismic	-297.94	-197.76	197.76	-197.76	197.76	297.76
Gravity	63.34	126.67	-126.67	-126.67	126.67	63.34
Combined	-243.60	-71.10	71.10	-324.43	324.43	361.28

A.3 Designing the Reversing Hinge Frames

Beam:

The beam yield moments were taken at the intersection of the column faces.

Beam-column Model:

$$M_{face} = 182.052 \text{ kNm}$$

Hinge Model:

$$M_{face} = 182.052 \text{ kNm}$$

Strain hardening values were calculated as outlined previously.

Beam-column Model:

$$\alpha = \frac{3.75 \times 185.052 \times \dfrac{3.275}{2}}{3 \times 2.935 \times 10^{7} \times 4.627 \times 10^{-3}} = 0.00279$$

Hinge Model: -steel element

$$\alpha = \frac{3.75 \times 185.052 \times 0.02 \times 15}{0.54^{2} \times 2 \times 10^{8} \times 2.328 \times 10^{-3}} = 0.001533$$

The hinge properties were calculated according to the rules defined previously.

1. $A_s d^2 n \geq I$

$$\rightarrow A_s = \frac{4.6273 \times 10^{-3}}{0.54^{2} \times \dfrac{2 \times 10^{8}}{2935 \times 10^{4}}}$$

$$= 2.328 \times 10^{-3} \text{ m}^2$$

2. $f_y = (M / A_s d)$

$$= \frac{185.052}{2.328 \times 10^{-3} \times 0.54}$$

$$= 147.203 \times 10^{3} \text{ kPa}$$

3. $A_c \geq 0.5\ (0.6 \times 0.4 + 0.45 \times 0.075)$

$\rightarrow A_c = 0.1369\text{m}^2$

Columns:

The column yield moments were calculated according to the NZS 3101 code [9]. Yielding was prevented at the top of the columns.

$$\begin{aligned} M_{base} &= 297.9 \times \phi_o \times \omega \\ &= 297.9 \times 1.4 \times 1.0 \\ &= 417.120 \text{ kNm} \end{aligned}$$

Strain hardening was calculated as outlined previously.

$$\alpha = \frac{3.75 \times 297.943 \times 3.4}{3 \times 2.935 \times 10^7 \times 0.003417} = 0.012626$$

A.4 Designing the Uni-Directional Hinge Frames

Beam:

The beam yield moments were calculated in the span and at the column faces. The following results were obtained by interpolation;

$$M_{face} = 280.241 \text{ kNm}$$

$$M_{span} = 164.948 \text{ kNm.}$$

The strain hardening values were calculated again as outlined previously.

Beam-column:

$$\alpha_{face} = \frac{3.75 \times 280.241 \times 1.8167}{3 \times 2.935 \times 10^7 \times 4.627 \times 10^{-3}} = 0.00469$$

$$\alpha_{span} = \frac{1 \times 164.948 \times 2.826}{3 \times 2.935 \times 10^7 \times 4.627 \times 10^{-3}} = 0.00114$$

Hinge: - steel element

$$\alpha_{face} = \frac{3.75 \times 280.241 \times 0.02 \times 15}{0.54^2 \times 2 \times 10^8 \times 3.955 \times 10^{-3}} = 0.00137$$

$$\alpha_{span} = \frac{1 \times 164.948 \times 0.02 \times 15}{0.54^2 \times 2 \times 10^8 \times 2.328 \times 10^{-3}} = 0.00036$$

The hinge properties were calculated according to the rules defined previously.

Span hinge properties:

1. $A_s d^2 n \geq I$

$$\rightarrow A_s = \frac{4.6273 \times 10^{-3}}{0.54^2 \times \dfrac{2 \times 10^8}{2935 \times 10^4}}$$

$$= 2.328 \times 10^{-3} \text{ m}^2$$

2. $f_y = \dfrac{M_{span}}{A_s d}$

$$= \frac{164.948}{2.328 \times 10^{-3} \times 0.54}$$

$$= 131.211 \times 10^3 \text{ kPa}$$

3. $A_c \geq 0.5(0.6 \times 0.4 + 0.45 \times 0.075)$

$$\rightarrow A_c = 0.1369 \text{ m}^2$$

Column face hinge properties:

1. $f_y = 131.211 \times 10^3$

   (to be consistent with span hinge calculations)

2. $A_s = \dfrac{M_{col}}{f_y d}$

$= \dfrac{280.241}{131.211 \times 10^3 \times 0.54}$

$= 3.955 \times 10^{-3}\ m^2$

3. $A_c \geq 0.5\ (\ 0.6 \times 0.4 + 0.45 \times 0.075\ )$

$\rightarrow A_c = 0.1369\ m^2$

Columns:

Once again the column yield moments were calculated according to the NZS 3101 code [10]. Yielding was prevented at the top of the columns.

$$M_{base} = 361.3 \times \phi_o \times \omega$$
$$= 361.3 \times 1.4 \times 1.0$$
$$= 505.80\ kNm$$

Strain hardening was calculated as outlined previously.

$$\alpha = \frac{3.75 \times 505.795 \times 3.4}{3 \times 2.935 \times 10^7 \times 0.003417} = 0.02143$$

Appendix B

MULTI-STOREY FRAME DESIGN

B.1 Assumptions

1. The multi-storey frame was sized to satisfy seismic related stiffness requirements in the draft code.
2. Torsional effects were not considered so the analysis could be carried out on a two dimensional frame.
3. Initial yield strengths used in the analysis were calculated using the Draft Loadings Code. The yield strengths which could form in a real structure due to the application of minimum steel quantities required by the steel code were not taken into account.
4. The concrete strength was assumed to be 30 MPa at 28 days and to have an average strength within the structure of 39 MPa. The elastic modulus was taken to be 29350 MPa and the shear modulus as 11740 MPa.
5. The multi-storey frame was assumed to be part of a 3-bay, 6 storey building which has a seismic mass per floor of 5100 kN [14].
6. The strain hardening of the steel within the columns was assumed to be 10% for all column yield moment calculations.
7. P-Delta effects were not considered.

B.2 Design

B.2.1 Member Properties and Loading

In order to facilitate the multi-storey frame design, it was decided to retain the same member properties and loading values as those established for the portal frame.

B.2.2 Equivalent Static Seismic Force

The following results were obtained from the DRAIN-2DX eigenvalue analysis:

The periods of the first two modes;

$$T_1 = 0.82908\text{s} \quad T_2 = 0.23431\text{s}$$

The horizontal ductility one displacement;

$$x_{\mu=1} = 0.01695 \text{ m.}$$

Five percent damping was assumed for both modes in order to calculate the following damping factors:

The mass proportional damping factor;

$$A = \frac{2\omega_1\omega_2(\omega_1\xi_2 - \omega_2\xi_1)}{(\omega_1^2 - \omega_2^2)}$$

$$= \frac{-390.943}{-661.647}$$

$$= 0.5909$$

The initial stiffness damping factor;

$$B = \frac{2(\xi_1\omega_1 - \xi_2\omega_2)}{(\omega_1^2 - \omega_2^2)}$$

$$= \frac{-1.9237}{-661.647}$$

$$= 0.0029$$

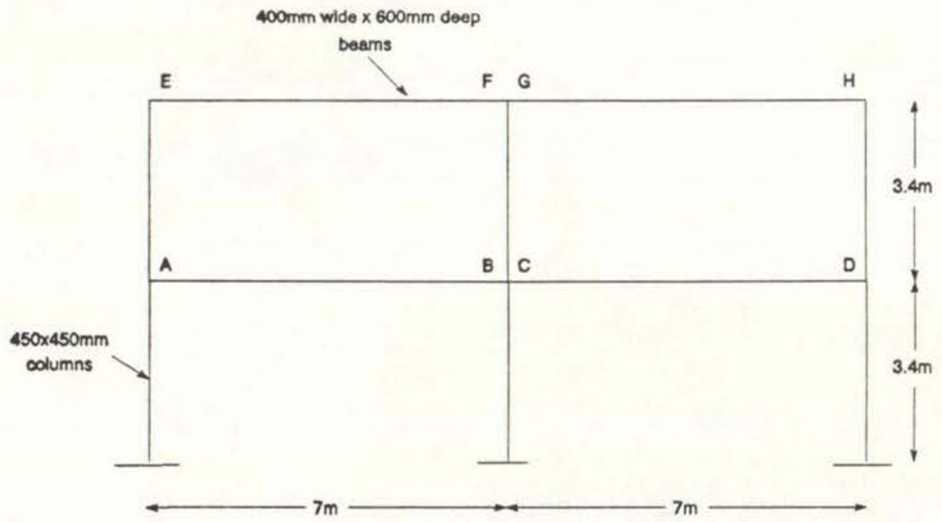

Fig. B.1 Position of Beam Bending Moments

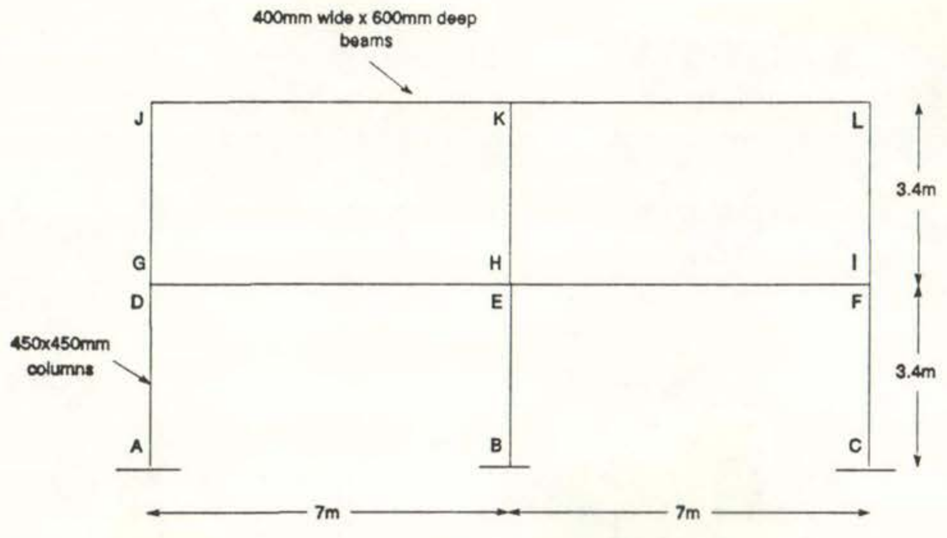

Fig. B.2 Position of Column Bending Moments

From the Draft Loadings Code [10] for a normal soil in the Wellington region and a design ductility of six:

$$C_o = 0.106651$$

$$\begin{aligned} C_d &= C_o R Z \\ &= 0.10655 \times 1.0 \times 0.8 \\ &= 0.08532 \end{aligned}$$

Thus the seismic base shear:

$$\begin{aligned} V &= C_d \times W_G \\ &= 0.08532 \times 6800 \\ &= 580.18 \text{ kN} \end{aligned}$$

Therefore the equivalent static lateral forces to be applied at each floor are:

$$F_{\text{level } i} = 0.92\ V \frac{W_i h_i}{\sum W_i h_i} \quad (+\ 0.08\ V \text{ for the roof only})$$

where:

$$\begin{aligned} W_{\text{level 1}} &= W_{\text{level 2}} = 3400 \text{ kN} \\ h_{\text{level 1}} &= 3.4 \text{ m} \\ h_{\text{level 2}} &= 6.8 \text{ m} \end{aligned}$$

Thus,

$$F_{\text{level 1}} = 177.92 \text{ kN}$$

$$F_{\text{level 2}} = 402.26 \text{ kN}$$

B.2.3 Strain Hardening and Hinge Structure Property Rules

The rules associated with the strain hardening of the elements and the hinge structure properties are the same as those employed for the portal frame design.

B.2.4 Design Moments

The following bending moment values were obtained from the DRAIN-2DX Response Spectrum analysis and the PFRAME gravity analysis. The values displayed are representative of the moments found at the centre-lines of the beam column intersections. Tables B.1 and B.2 illustrate the beam and column bending moments respectively. Figs. B.1 and B.2 show the positions on the frames that the points A through to L refer to.

Table B.1 Beam Bending Moments

Moment kNm	Mode One	SRSS	Gravity	SRSS+Grav.
A	-310.9	-310.90	-163.05	-473.95
B	285.30	285.34	-185.33	100.00
C	-285.30	-285.34	-185.33	-470.67
D	310.90	310.90	-163.05	147.85
E	-177.74	-181.71	-137.47	-318.18
F	160.82	163.85	-198.00	-34.15
G	-160.82	-163.85	-198.00	-361.85
H	177.74	181.71	-137.47	44.24

Table B.2 Column Bending Moments

Moment kNm	Mode One	SRSS	Gravity	SRSS+Grav.
A	-321.00	-324.32	-27.99	-352.31
B	-368.56	-371.78	0.00	-371.78
C	-321.00	-324.32	27.99	-296.33
D	-207.67	-215.15	-55.72	-270.87
E	-307.98	-314.20	0.00	-314.20
F	-207.67	-215.15	55.72	-159.43
G	-103.62	-120.62	-107.33	-227.95
H	-262.62	-272.33	0.00	-272.33
I	-103.62	-120.62	107.33	-13.29
J	-177.73	-182.44	-137.47	-319.91
K	-321.65	-327.79	0.00	-327.80
L	-177.73	-182.44	137.47	-44.97

B.3 Designing the Reversing Hinge Frames

Beams:

The beam properties were calculated according to the rules described in Appendix A where:

$$A_s d^2 n \geq I_{section}$$

$$f_y = \frac{M_i}{A_s d}$$

$$A_c \geq 0.5 A_{section}$$

$$\alpha = \frac{\beta M_i \ell_{eff}}{d^2 E_s A_s}, \quad \text{for hinge steel elements}$$

$$\alpha = \frac{\beta M_i \ell_{eff}}{3EI}, \quad \text{for yielding beam-column elements}$$

Table B.3 illustrates the element properties employed in the frame analyses and calculated using the equations described above.

Table B.3 Beam Element Properties

		Level 1	Level 2
Hinges at External Column Faces	M_i	291.78 kNm	170.6 kNm
	A_s	0.002328 m^2	0.002328 m^2
	f_y	233 x 10^3 kPa	136 x 10^3 kPa
	A_c	0.1369 m^2	0.1369 m^2
	$\alpha_{\text{steel element}}$	0.002418	0.0014136
	$\alpha_{\text{beam-column element}}$	0.004398	0.002571

Hinges at Internal Column Faces	M_i	266.18 kNm	152.74 kNm
	A_s	0.002328 m^2	0.002328 m^2
	f_y	212 x 10^3 kPa	121 x 10^3 kPa
	A_c	0.1369 m^2	0.1369 m^2
	α_{steel} element	0.0022056	0.001266
	$\alpha_{beam\text{-}column}$ element	0.004012	0.002302

Columns:

The column yield moments were calculated according to the NZS 3101 code [9].

$$M_{design} = \phi_o \, \psi \, M_{mode\ 1}$$

where:

$$\phi_o = \text{beam overstrength factor}$$

$$= \frac{1.1 \text{ x} \sum M_{beam:\ SRSS}}{\sum M_{column:\ mode\ 1}} \text{ (levels 1 and 2)}$$

$$= 1.4 \text{ (ground level)}$$

$$\omega = \text{dynamic magnification factor}$$

$$= 1.0 \text{ (ground level and level 2)}$$

$$= 1.3 \text{ (level 1)}$$

The results of these calculations are illustrated in Table B.4.

Table B.4 Column Design Moment Calculations

External Columns					
$\Sigma M_{col:mode\ 1}$	$M_{beam:SRSS}$	ϕ_o	ω	$M_{col\ centre\ line}$	$M_{col\ face}$ kNm
177.73	181.7	1.125	1.0	199.95	158
310.95	310.9	1.1	1.3	296.42	255
321.0	-	1.4	1.0	449.40	450
Internal Columns					
$\Sigma M_{col:mode\ 1}$	$M_{beam:SRSS}$	ϕ_o	ω	$M_{col\ centre\ line}$	$M_{col\ face}$ kNm
321.65	327.7	1.12	1.0	360.24	290
570.60	570.68	1.1	1.3	440.40	370
368.56	-	1.4	1.0	515.98	516

The strain hardening of the columns was calculated according to the rules discussed in Appendix A:

$$\alpha = \frac{\beta M \ell_{eff}}{3EI}$$

where β = 3.75

ℓ_{eff} = 3.4 m

E = 2.935×10^5 MPa

I = 0.003417 m^4

M_i = $M_{column\ face}$

The column strain hardening values obtained are shown in Table B.5.

Table B.5 Column Strain Hardening Values

		External Columns α values	Internal Columns α values
Level 2		0.0067	0.0123
Level 1	Top	0.0108	0.0157
	Bottom	0.0108	0.0157
Ground		0.0191	0.0219

B.4 Designing the Uni-directional Hinge Frames

Beams:

In order to calculate the beam properties it was first necessary to determine the maximum span moment and where it occurred. Hence, the following calculations were carried out:

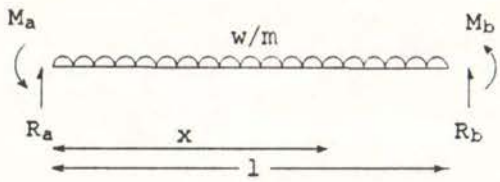

Fig. B.3 Schematic Drawing for Maximum Span Moment Calculations

$$R_B = \frac{\left(-M_A - M_B + \frac{\omega L^2}{2}\right)}{L}$$

The maximum moment occurs at zero shear therefore:

$$x = \frac{R_A L}{\omega L} = \frac{R_A}{\omega}$$

Thus the magnitude of the maximum moment is given by:

$$M_{max} = -M_A + R_A x - \frac{\omega x^2}{2}$$

Table B.6 illustrates the values obtained using the above equations in order to calculate the maximum span moments.

Table B.6 - Maximum Span Moment Calculations

	M_A	M_B	R_A	R_B	x	M_{span} (kNm)
Level 2	361.854	44.293	202.57	86.53	4.905	134.94
Level 1	470.67	147.85	232.91	56.19	5.639	186.08

Thus the beam properties could be calculated according to the rules described in Appendix A:

$$A_s d^2 n \geq I_{section}$$

$$f_y = \frac{\text{Mid face}}{A_s d}$$

$$A_c \geq 0.5\ A_{section}$$

$$\alpha = \frac{\beta\, M_i\, \ell_{eff}}{d^2 E_s A_s}, \quad \text{for hinge steel elements.}$$

$$\alpha = \frac{\beta\, M_i\, \ell_{eff}}{3EI}, \quad \text{for yielding beam-column elements.}$$

Table B.7 gives the element properties employed in the frame analyses and calculated using the above equations.

Table B.7 - Beam element properties.

		Level 1	Level 2
Hinges at Column Faces	M_i	419.31 kNm	317.321 kNm
	A_s	0.002328 m^2	0.002328 m^2
	f_y	333 x 6 x 10^3 kPa	251 x 4 x 10^3 kPa
	A_c	0.1369 m^2	0.1369 m^2
	α_{steel} element	0.00347	0.00263
	$L_{eff\ beam\text{-}column}$ element	2.412 m	2.124 m
	$\alpha_{beam\text{-}column}$ element	0.004398	0.002571
Span Hinges	M_i	186.077 kNm	134.94 kNm
	A_s	0.002328 m^2	0.002328 m^2
	f_y	148.0 x 10^3 kPa	107.3 x 10^3 kPa
	A_c	0.1369 m^2	0.1369 m^2
	α_{steel} element	0.000411	0.000298
	$L_{eff\ beam\text{-}column}$ element	3.002 m	2.556 m
	$\alpha_{beam\text{-}column}$ element	0.004012	0.000847

Columns:

Once again the column yield moments were calculated according to the NZS 3101 code [9].

$$M_{design} = \phi_o \psi M_{mode\ 1}$$

where:

ϕ_o = beam overstrength factor

$$= \frac{1.1 \times \sum M_{beam:\ SRSS+\ gravity}}{\sum M_{column:\ mode\ 1}} \text{ (levels 1 and 2)}$$

= 1.4 (ground level)

ω = dynamic magnification factor

= 1.0 (ground level and level 2)

= 1.3 (level 1)

Table B.8 shows the results of these calculations.

Table B.8 Calculations for Column Face Design Bending Moments

External Columns					
$\Sigma M_{col:mode\ 1}$	$M_{beam:SRSS}$	ϕ_o	ω	$M_{col\ centre\ line}$	$M_{col\ face}$ kNm
177.74	319.18	1.975	1.0	351.02	281
311.25	473.95	1.675	1.3	452.11	382
321.0	-	1.4	1.0	449.40	450
Internal Columns					
$\Sigma M_{col:mode\ 1}$	$M_{beam:SRSS}$	ϕ_o	ω	$M_{col\ centre\ line}$	$M_{col\ face}$ kNm
321.65	327.70	1.121	1.0	360.57	290
570.60	570.67	1.10	1.3	440.40	370
368.56	-	1.4	1.0	515.98	516

The strain hardening of the columns was calculated according to the rules discussed in Appendix A:

$$\alpha = \frac{\beta M_i \ell_{eff}}{3EI}$$

where:

β = 3.75

ℓ_{eff} = 3.4 m

E = 2.935×10^7 MPa

I = 0.003417 m^4

M = column face design moment

The strain hardening values obtained are shown in Table B.9.

Table B.9 - Column Strain Hardening Values.

		α for External Columns	α for Internal Columns
Level 2		0.0067	0.0123
Level 1	Top	0.0162	0.0157
	Bottom	0.0162	0.0157
Ground		0.0191	0.0219